The Meteoritical Society

Meteoritics & Planetary Science 1–29 (2023)
doi: 10.1111/maps.14111

Investigating the impact of x-ray computed tomography imaging on soluble organic matter in the Murchison meteorite: Implications for Bennu sample analyses

Daniel P. GLAVIN[1]*, Scott A. ECKLEY[2], José C. APONTE[1], Eve L. BERGER[3], Aaron S. BURTON[3], Jason P. DWORKIN[1], Jamie E. ELSILA[1], Frank T. FERGUSON[1,4], Yoshihiro FURUKAWA[5], Heather V. GRAHAM[1], Toshiki KOGA[6], Michael LISS[7], Hannah L. MCLAIN[1,4], Hiroshi NARAOKA[8], Yasuhiro OBA[9], Eric T. PARKER[1], Kevin RIGHTER[3], Philippe SCHMITT-KOPPLIN[7], Danielle N. SIMKUS[1,4], Yoshinori TAKANO[6], Harold C. CONNOLLY Jr.[10,11,12], and Dante S. LAURETTA[11]

[1]Solar System Exploration Division, NASA Goddard Space Flight Center, Greenbelt, Maryland, USA
[2]Jacobs Technology, NASA Johnson Space Center, Houston, Texas, USA
[3]Astromaterials Research and Exploration Science Division, NASA Johnson Space Center, Houston, Texas, USA
[4]Department of Chemistry, Catholic University of America, Washington, DC, USA
[5]Department of Earth Science, Tohoku University, Sendai, Japan
[6]Biogeochemistry Research Center, Japan Agency for Marine-Earth Science and Technology, Yokosuka, Japan
[7]Research Unit Analytical Biogeochemistry, Helmholtz Munich, Neuherberg, Germany
[8]Department of Earth and Planetary Sciences, Kyushu University, Fukuoka, Japan
[9]Institute of Low Temperature Science, Hokkaido University, Sapporo, Japan
[10]Department of Geology, School of Earth and Environment, Rowan University, Glassboro, New Jersey, USA
[11]Lunar and Planetary Laboratory, University of Arizona, Tucson, Arizona, USA
[12]Department of Earth and Planetary Science, American Museum of Natural History, New York, New York, USA

***Correspondence**
Daniel P. Glavin, Solar System Exploration Division, NASA Goddard Space Flight Center, 8800 Greenbelt Road, Code 690, Greenbelt, MD 20771, USA.
Email: daniel.p.glavin@nasa.gov

(Received 22 May 2023; revision accepted 27 November 2023)

Abstract–X-ray computed tomography (XCT) is a valuable reconnaissance tool for three-dimensional imaging and identification of distinct lithologies in extraterrestrial samples. It will be used as part of the preliminary examination of samples returned from asteroid (101955) Bennu by the Origins, Spectral Interpretation, Resource Identification, and Security–Regolith Explorer (OSIRIS-REx) mission. However, it must first be established whether x-rays generated during XCT could degrade or alter the organic composition of the returned samples by radiolysis. To test this, we split a crushed sample of the Murchison CM2 meteorite, kept one portion as a control, and irradiated the other portion up to the maximum x-ray dosage (~180 Gy) that a Bennu sample would experience during an XCT imaging experiment. We then extracted organic compounds from both splits and conducted (i) nontargeted soluble organic analyses to compare the chemical distributions of C-, H-, O-, N-, and S-bearing species and (ii) targeted measurements to quantify the abundances of 96 individual soluble organic molecules that included protein amino acids, amines, carboxylic acids, hydroxy acids, carbonyl compounds, polycyclic aromatic hydrocarbons, alcohols, sugars, and N-heterocycles. We found that XCT imaging of the Murchison meteorite had no measurable impact on the relative abundances or enantiomeric compositions of most of the soluble organic compounds targeted in this study. Elevated total abundances of several soluble organic compound classes were observed in the XCT-scanned Murchison sample relative to the control. This is likely related to particle size heterogeneity and specific surface area differences between the sample aliquots used for the extractions, rather than a result of

the x-ray exposure. Assuming the samples returned from asteroid Bennu by OSIRIS-REx have a similar composition to carbonaceous chondrites, these data provide confidence that XCT will not significantly alter their soluble organic compositions.

INTRODUCTION

X-ray computed tomography (XCT) measurements are increasingly being used for three-dimensional (3-D) reconnaissance imaging of meteorites and returned samples to aid in the characterization of lithologies through the identification of internal structural components such as voids, veins, or other petrographic features prior to sample processing or subdivision for detailed petrographic, mineralogical, and chemical analyses (Ebel & Rivers, 2007; Friedrich et al., 2013, 2014). The Origins, Spectral Interpretation, Resource Identification, and Security–Regolith Explorer (OSIRIS-REx) mission delivered samples of regolith from asteroid (101955) Bennu in September 2023 (Lauretta et al., 2022). Observations by the OSIRIS-REx spacecraft have confirmed that Bennu is a carbonaceous B-type asteroid that exhibits a hydration feature in the 3 μm region that is spectrally similar to those of aqueously altered CI- and CM-type chondrites (e.g., Hamilton et al., 2019; Simon et al., 2020). In addition, on the asteroid surface significant surficial diversity exists consisting of distinct lithologies (DellaGiustina et al., 2020; Lauretta et al., 2019; Rozitis et al., 2020), including boulders with carbonate veins (Kaplan et al., 2020) and exogenous materials, likely from asteroid Vesta (DellaGiustina et al., 2021). Therefore, it is possible that the samples returned by OSIRIS-REx could contain mixtures of distinct lithologies, embedded veins, or other hidden features that should be identified by XCT. Results from the 3-D scanning can be used to isolate different lithologies prior to sample powdering and homogenization that is a necessary preparation for bulk elemental analyses as well as soluble organic measurements.

XCT imaging is generally considered a nondestructive technique because silicate and metallic minerals in chondrites are not affected by x-rays at the intensities and wavelengths that have been used to investigate the density structure of a variety of meteorites and their components in three dimensions, including chondrules, metal and sulfide grains, and calcium-aluminum inclusions (e.g., Ebel & Rivers, 2007 and references therein). However, XCT can alter and even eradicate the natural radiation history of chondrites as measured by thermoluminescence (Sears et al., 2016, 2018). Before exposing a sample to x-ray radiation, it is important to be aware of any effects that could impact the results or interpretation of data from subsequent analyses.

Analysis of the distribution and relative abundance (abundance of a specific organic molecule relative to the abundance of another organic compound of the same molecular class in the same sample, expressed as a ratio) of organic compounds in meteorites and returned samples can provide information about their formation mechanisms, parent body alteration conditions, and the degree of terrestrial organic contamination (Glavin et al., 2018). Therefore, it is crucial to understand whether x-ray radiation could alter the organic composition of extraterrestrial materials—in particular soluble organic molecules, such as amino acids and N-heterocycles, that can decompose by radiolysis when exposed to ionizing radiation at elevated doses in the range of ~0.1 MGy or more (Ertem et al., 2021; Hammer et al., 2019; Kminek & Bada, 2006; Pavlov et al., 2022), although many N-heterocycles show little degradation when irradiated in the solid state with gamma at room temperature up to a total dose of ~1 MGy (Hammer et al., 2019).

Experimental studies investigating the impact of ionizing radiation on macromolecular organic material in terrestrial samples have found evidence for alteration via cross-linking, oxidation, and bond scission (Court et al., 2006; Schafer et al., 2009). For aqueously altered CI- and CM-type carbonaceous chondrites, key analogs for the returned sample from Bennu, there have been only a limited number of experimental studies of the impact of x-rays on organic matter within these meteorites. Previous experiments with the Murchison meteorite have shown that polychromatic XCT and synchrotron XCT imaging up to a total dose of ~3 kGy do not alter the abundances of amino acids or their enantiomeric ratios after x-ray exposure (Friedrich et al., 2016, 2019). Nevertheless, the impact of XCT at any dose on other soluble organic compound classes that are also present in Murchison and other carbonaceous meteorites is unknown.

To test the impact of XCT on soluble organics and evaluate the suitability of this technique for preliminary examination of the Bennu samples, we conducted an experiment on a sample of the Murchison meteorite that was split into an XCT-imaged portion and a control portion. The Murchison CM2 carbonaceous chondrite was selected for this study because asteroid Bennu is thought to be compositionally similar to aqueously altered CM meteorites (Hamilton et al., 2019), the organic composition of Murchison has been studied extensively (Glavin et al., 2018), and the meteorite contains a highly diverse mixture of soluble organic compounds

(Schmitt-Kopplin et al., 2010), which is of particular interest in understanding whether x-rays can affect their overall abundance and, by extraction, those that may be contained within Bennu samples.

The focus of this paper is on comparing the abundances and distributions of soluble organic compounds in the solvent extracts of the XCT-imaged sample with those in the non-irradiated control sample. We thus do not discuss the formation mechanisms or extent of terrestrial contamination of the organic compounds identified. In addition to the XCT experiment, we validated extraction and analytical techniques that could be used on the Bennu samples but that had not yet been tested on carbonaceous meteorites. Therefore, we also include protein amino acid, amine, and alcohol data from the irradiated and control Murchison samples.

MATERIALS AND METHODS

Meteorite Processing Procedures

All glassware, ceramics, and sampling handling tools used in sample processing were rinsed with Millipore Milli-Q Integral 10 ultrapure water (18.2 MΩ·cm, ≤ 3 ppb total organic carbon; hereafter referred to as "water"), wrapped in aluminum foil, and then heated in a furnace at 500°C in air for 18 h to remove any organic contamination. Four centimeter-sized fragments of the Murchison meteorite (USNM 5453,1; total mass = 10.3 g) allocated by the Smithsonian National Museum of Natural History in Washington, DC, were sealed inside two separate clear borosilicate glass vials with aluminum foil–lined caps and shipped to the soluble organics in Astromaterials Laboratory at the NASA Johnson Space Center (JSC) for further sample preparation. At JSC, the Murchison meteorite chips were then transferred from the glass vials into a large porcelain mortar and lightly crushed by hand to smaller fragments by tapping the particles with a porcelain pestle inside a positive pressure ISO 5 HEPA-filtered laminar flow clean bench. Approximately 1 g of the crushed Murchison meteorite, which consisted of a few millimeter-sized particles and a single 0.5 g chip, was then removed from the mortar for other OSIRIS-REx experiments that were not part of this XCT study. The remaining coarse-grained Murchison material inside the mortar was further ground down by hand with a pestle until no visible fragments could be observed in the dark powder.

After grinding, the crushed meteorite sample was then transferred from the porcelain mortar to a 12 mL clear borosilicate glass vial through a glass funnel by scraping the material from the mortar with a stainless steel spatula. The glass vial containing the Murchison sample was weighed (total mass of Murchison ~9.3 g) and then placed on a vortex mixer for 3 min to further mix and homogenize the sample (Figure 1). It is possible that some particle size sorting of the Murchison sample occurred during this vortex mixing step, with larger particles migrating toward the top of the vial (e.g., the Brazil nut effect). The crushed Murchison sample was not sieved to minimize the risk of organic contamination.

After vortex mixing, the Murchison sample was split into two approximately equal mass portions and transferred into separate 12 mL clear glass vials labeled Murchison A (mass = 4.6646 g) and Murchison B (mass = 4.6430 g). The Murchison B sample vial was sealed inside a curation clean Teflon bag with Teflon tape, then rolled up in the Teflon bag and provided to the Astromaterials x-ray Fluorescence and Computed Tomography (X-FaCT) Laboratory at NASA JSC for the 3-D XCT imaging experiment. The Murchison A sample was used as a control and kept under similar environmental conditions as the Murchison B sample but was not exposed to any experimental x-rays from the XCT scan. To conduct a blind test, the analysts were not told which sample was irradiated before their analyses.

XCT Parameters Used for the Murchison Meteorite

The XCT 3-D imaging of the crushed Murchison B sample aliquot was performed using a Nikon XTH 320 lab-based system (i.e., not synchrotron) at JSC, which is well suited for scanning a wide variety of sample types and sizes from ~0.5 mm up to 15 cm (Eckley et al., 2020; Wilbur et al., 2023). The instrument is equipped with a 180 kV nano-focus tungsten transmission source (spot size ~1 μm up to 3.0 W power) that produces a polychromatic x-ray beam and a 2000 × 2000 pixel Perkin Elmer flat panel charge-coupled device (CCD) detector. For the Murchison B XCT scan, the x-ray tube energy (i.e., filament voltage) was set to 160 kV and the filament current was set to 38 μA, which produced a polychromatic x-ray beam with photon energies up to 160 keV. A low-energy x-ray beam filter, which is commonly used to reduce beam-hardening artifacts, was intentionally not used in this XCT experiment to expose the Murchison sample to as large a range of x-ray energies as possible. The sample was imaged through a continuous 360° rotation collecting 3141 radiographs (i.e., 2-D x-ray absorption image) at every 0.115° with eight frames averaged per radiograph at 1.00 s exposure per frame. The total time (scan time plus time to align and center the sample) that the sample was exposed to the x-ray beam was 500.5 min (8.3 h). The distance between the x-ray source and center of the sample was 39.22 mm and the distance between the x-ray source and detector was 679.51 mm. This configuration produced a reconstructed cubic voxel (i.e., pixel with third dimension) size of 11.54 μm/voxel edge.

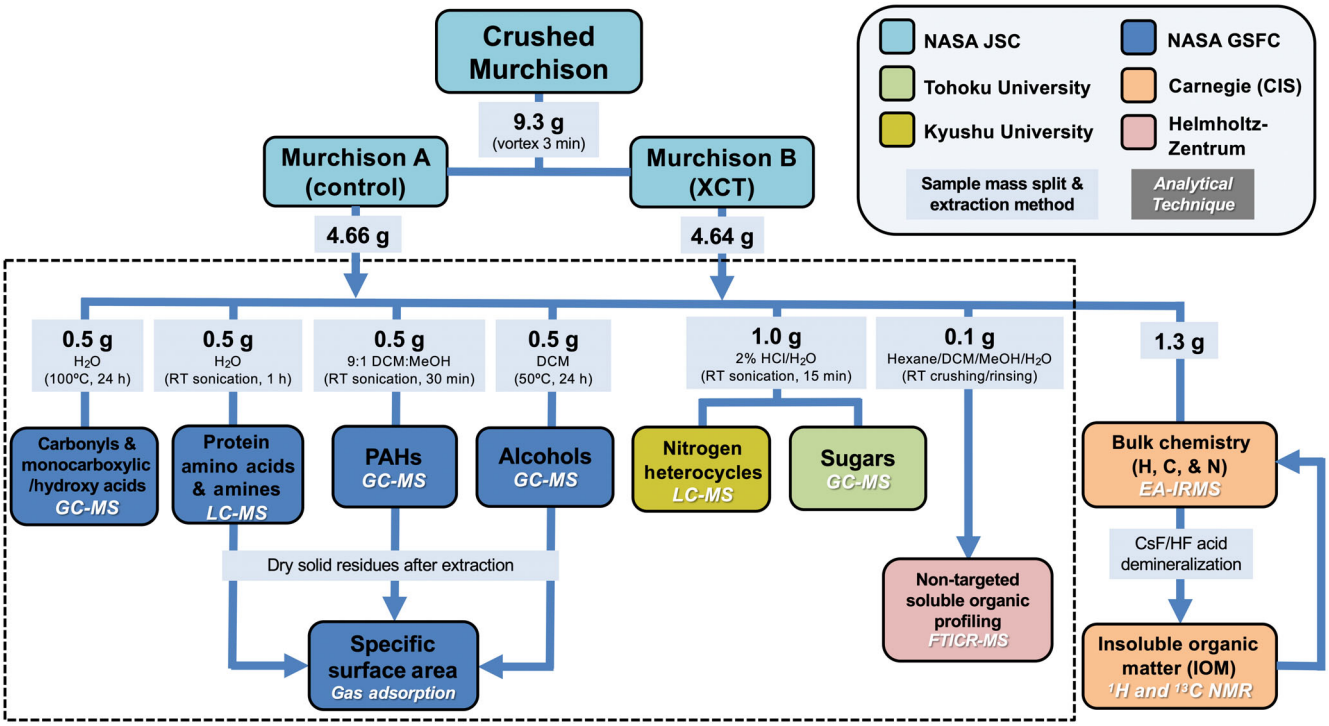

FIGURE 1. Scheme for the sample allocation and analysis flow of the Murchison A (control) and Murchison B (XCT) samples. The targeted and non-targeted soluble organic molecule analyses of the Murchison extracts and the specific surface area measurements of the residues reported in this paper are shown inside the dashed box. The institutions where the sample processing and analysis steps were performed are indicated by color. The masses shown in the light blue boxes used for the soluble organic analyses represent the amount of sample used from each of the Murchison A and Murchison B sample vials originally containing ~4.6 g of material.

Meteorite Sample Allocation and Analysis Scheme

The Murchison meteorite allocation and analysis scheme used in this study are illustrated in Figure 1. Following the XCT imaging experiment of Murchison B, individual aliquots of roughly equivalent volume were scooped from both the Murchison A (non-irradiated control sample) and Murchison B (XCT-imaged sample) vials and transferred into smaller clean glass vials using a metal spatula inside a HEPA-filtered laminar flow bench at NASA JSC. The Murchison A and B sample portions were then weighed using a mass balance, and the sample vials were covered with a small piece of baked-out aluminum foil before sealing in air with a plastic screw cap with a PTFE liner. The individual A and B sample vials were then sent to multiple institutions for extraction and analysis to determine the abundances and distributions of soluble organic compounds using both targeted and nontargeted methods (Figure 1). The detailed descriptions of the reagents and standards, sample extraction, purification and derivatization procedures, and the instrument conditions and quantification methods used for the soluble organic analyses are given in the Supporting Information.

To briefly summarize the methods used, ~2 g each of Murchison A and B was split into 0.5 g portions at NASA Goddard Space Flight Center (GSFC) for the extraction and analysis of carbonyl compounds (aldehydes and ketones), carboxylic acids, hydroxy acids, protein amino acids, amines, polycyclic aromatic hydrocarbons (PAHs), and alcohols. The carboxylic acids, hydroxy acids, and carbonyl compounds were extracted from the Murchison A and B sample portions by heating in water at 100°C for 24 h and the water extracts were then derivatized and analyzed by gas chromatography triple-quadrupole mass spectrometry (GC-QqQ-MS).

The protein amino acids and amines were extracted from the Murchison samples using a new method that involves sonication in water at room temperature for 1 h followed by derivatization of the water extract and analysis using liquid chromatography with ultraviolet (UV) fluorescence and triple-quadrupole mass spectrometry (LC-FD/QqQ-MS) detection. The PAHs were extracted from the Murchison samples by sonication in a dichloromethane (DCM) and methanol mixture (9:1 v/v) at room temperature for 30 min followed by extract purification and direct analysis using GC-QqQ-MS. The alcohols were extracted from Murchison in

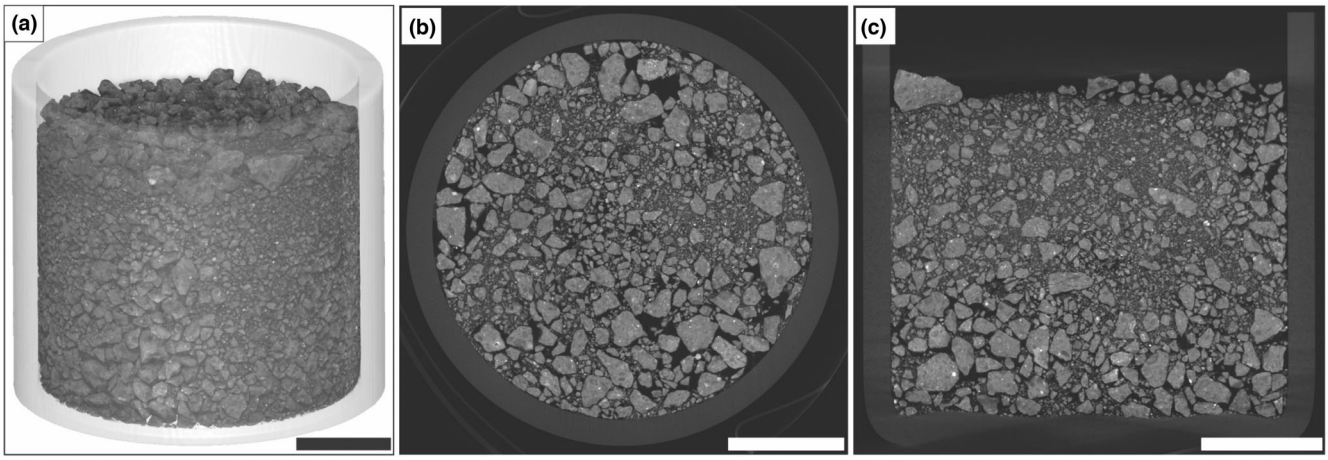

FIGURE 2. (a) 3-D volume rendering of the crushed Murchison B sample in the glass vial from the XCT data. The glass vial is rendered semitransparent, and the Murchison material is rendered opaque. (b) Top-down and (c) side-view grayscale CT slices (2-D TIFF images). The scale bars shown at the bottom right of each image are 5 mm. Videos of the CT slices (Figure S1) and 3-D volume rendering (Figure S2) can be found in the Supporting Information.

DCM using a new method by heating at 50°C for 24 h and the extracts were then derivatized and analyzed by GC-QqQ-MS.

At Tohoku University in Japan, ~1 g portions from each of the Murchison A and B samples were extracted six times in water and 2% HCl by room temperature sonication for 15 min and then purified for the derivatization and analysis of sugars (pentoses) by gas chromatography mass spectrometry (GC–MS). Portions of the same Murchison water and 2% HCl extracts were also analyzed for N-heterocycles by high-performance liquid chromatography/high-resolution mass spectrometry (HPLC-HRMS) at Kyushu University in Japan.

Approximately 0.1 g of each Murchison sample was also sent to Helmholtz-Zentrum in Munich, Germany, for sequential extraction in hexane, DCM, methanol, and water and for nontargeted chemical profiling of the soluble organic matter (SOM) using Fourier transform ion cyclotron resonance-mass spectrometry (FTICR-MS). In addition, ~1.3 g each of the Murchison A and B samples was allocated to the Carnegie Institution for Science in Washington, DC, for bulk H, C, and N abundances and isotope ratios using an elemental analyzer-isotope ratio mass spectrometer (EA-IRMS) and solid-state ^{1}H and ^{13}C nuclear magnetic resonance (NMR) measurements of the Murchison insoluble organic matter (IOM). The experimental details and results from the bulk chemical analyses of the Murchison IOM are discussed elsewhere (Cody et al., 2023; Glavin et al., 2023).

Specific surface area measurements were made at NASA GSFC on three different sets of dried Murchison A and B solid residues obtained after solvent extraction of the protein amino acids and amines, PAHs, and alcohols, respectively, by nitrogen gas adsorption (Figure 1) using a Quantachrome NOVA 2200e surface area and pore size analyzer. This unit can measure two samples at a time, so the Murchison A and B sample residues from each extraction were run simultaneously as pairs. Nitrogen gas adsorption experiments were performed three times for each Murchison A and B residue pair to obtain the average and standard deviation error of the total surface area per unit of sample mass in square meters per gram (Table S1). Specific surface area measurements were not made on any Murchison samples before solvent extraction to minimize the potential for organic contamination of the samples. In addition, no surface area measurements were made on the Murchison residues after solvent extraction of the carbonyl compounds, monocarboxylic and hydroxy acids, N-heterocycles, and sugars because these solid residues were used for IOM and other analyses.

RESULTS AND DISCUSSION

Radiographs and Images from the XCT Scan

The 3141 radiographs collected during the XCT scan were mathematically reconstructed into a 2000 × 2000 × 2000 voxel 3-D volume (i.e., tomogram) using proprietary Nikon software (CTAgentPro v5.4) that implements a filtered backprojection algorithm. The 3-D volume was then exported as a continuous series of 2-D TIFF images (CT slices) oriented orthogonally to the scan rotation axis. A 3-D volume rendering of the powdered Murchison B sample, as well as top-down and side-view grayscale CT slices (TIFF images), is shown in Figure 2. Brighter objects shown in Figure 2 represent materials with a higher x-ray attenuation (i.e., higher atomic number and/or density). These images, as well as a video of the

continuous sequence of reconstructed CT TIFF slices (Figure S1) and another XCT video showing a 3-D volume rendering made from the reconstructed CT slices (Figure S2), demonstrate that the Murchison B sample was not homogenous with respect to particle size after crushing with a mortar and pestle. The powder contained a wide particle size distribution ranging from the scan resolution limits of ~30 μm (i.e., around 3× the voxel size) to approximately 2.8 mm, with an uneven spatial distribution defined by layering of large particles near the bottom of the glass vial and a central plug of fine-grained material (Figures 2, S1, and S2).

We cannot report the particle size distribution for the Murchison A sample because, as the control, it was not analyzed by XCT. Nevertheless, we can assume that the Murchison A sample also contained a similarly large range of particle sizes because it was taken from an equal-mass split of the same crushed material as Murchison B. Although we allocated roughly equal portions of sample mass from the Murchison A and B vials for the soluble organics analyses, it is possible that the individual sample aliquots sent to the institutions for analysis had different particle size distributions (and therefore different specific surface areas). This could have resulted in differences in the extraction efficiency of organic compounds between the paired Murchison A and B samples. To account for the particle size heterogeneity, as described previously, nitrogen gas adsorption measurements were made for some of the Murchison A and B sample sets after solvent extraction to determine the specific surface areas of the residues. As shown in Table S1, we observed statistically significant differences in the average specific surface areas of the Murchison A and B residue pairs after extraction for the analysis of amino acids and amines, PAHs, and alcohols.

Total X-Ray Dose Calculation

A precise calculation of the total radiation exposure of organic compounds in Murchison during the XCT experiment is difficult because SOM is not homogenously distributed within the meteorite and can be found along grain boundaries in minerals or even between layers of minerals within the chondritic matrix material (Becker & Epstein, 1982; Le Guillou & Brearley, 2014). In addition, impinging x-ray photons will interact with soluble organic molecules and their electrons and also with the surrounding mineral matrix and IOM, generating secondary electrons and x-rays, which in turn can interact with organic molecules. To compare the x-ray dose that the Murchison B sample experienced in our study to x-ray doses experienced by other Murchison samples in a similar study that also used a lab-based CT system with a polychromatic x-ray source (Friedrich et al., 2019), we estimated the total radiation dose using their same methods described below. It should be noted that we were not aiming for a specific dosage in this study, but rather to CT scan the Murchison B sample at conditions that are more extreme (i.e., longer scan duration, higher x-ray tube energy and current, and no filtering) than what Bennu samples will experience during preliminary examination using the same instrument. Up to 4 h of scan time are allotted per sample, and scan conditions have been determined based on CT scans of Bennu simulant that cover the range of expected returned sample sizes (x-ray tube energy and current will vary from 90 to 120 kV and 27 to 33 μA, respectively, and 0.1 to 0.25 mm of Al filtering).

To estimate the total x-ray dose, we first calculated a theoretical x-ray photon emission spectrum at 1 keV intervals for a tungsten x-ray tube set to 160 kV using SpekCalc software (Poludniowski et al., 2009). The predicted number of photons at each 1 keV interval was then multiplied by the tube current (38 μA), an estimated exposure cross section of 2.7 cm^2 of the Murchison B sample in the vial, the measured sample mass of 4.6430 g, total scan time of 8.3 h, and observation of the sample field of view showing that of the 4 million pixels that compose a single radiograph, only 57% of the pixels contained meteorite material that could interact with and absorb photons generated by the x-ray tube. The value at each kiloelectron volt was summed across all energy intervals to calculate the total energy transmitted to the Murchison B sample. This was divided by the sample mass to convert to the commonly used x-ray dosage unit of gray (Gy = 1 J kg^{-1}). The total x-ray dose experienced by the Murchison B sample was calculated to be ~180 Gy. This dose is lower than the 280–2800 Gy total exposures tested in previous polychromatic XCT imaging experiments of the Murchison meteorite (Friedrich et al., 2019). The dosage is also the maximum to which the returned samples would be exposed during an XCT scan at JSC as part of preliminary examination.

Although we did not directly measure the temperature of the Murchison sample in the vial during the XCT scan, the ambient temperature in the XCT laboratory at JSC ranged from ~20 to 24°C, and the ambient temperature inside the XCT cabinet is kept between 20 and 23°C using an internal air-conditioning/cooling system that is integrated into the system. Ambient temperatures in other laboratory-based XCT cabinets, like what was used by Friedrich et al. (2019), might vary from those of the JSC system but are generally designed to maintain temperatures around 25°C. Therefore, sample heating during the XCT scan from the ambient air is insignificant. Interactions between x-ray photons and the Murchison B sample are expected to impart a small amount of energy in the form of heat. Friedrich et al. (2016) estimated that the maximum theoretically possible sample temperature

increase above room temperature caused by interactions with x-rays is <2°C. Their estimation was based on the calculated total energy absorbed by the Murchison samples, which was significantly higher (1.1 and 1.2 kGy) than what the Murchison B sample experienced in this study (~180 Gy). Therefore, the temperature of the Murchison B sample did not exceed 26°C during the XCT scan.

The standard XCT experiment during Bennu preliminary examination of an ~2 g mass chip will use a 100 kV filament voltage and 30 μA current, 0.1–0.25 mm of aluminum filtering, 1 cm^2 sample cross section, absorption of 75% of the x-rays generated, and a 4-h total scan time, yielding a total x-ray dose of ~50 Gy. The 180 Gy total x-ray dose calculated for Murchison in this XCT study is approximately an order of magnitude less than those experienced by monochromatic synchrotron x-ray sources, such as the one at the Advanced Photon Source at Argonne National Laboratory used for the x-ray microtomography experiments of Murchison with x-ray doses of up to ~1.2 kGy (Friedrich et al., 2016). Similarly, the XCT scan conditions for Bennu materials are not expected to raise the sample temperature by more than 2°C.

Abundances of Targeted Soluble Organic Compound Classes

We determined the abundances in nanomoles per gram (nmol g^{-1}) of the individual soluble organic molecules identified to be above blank levels in the solvent extracts of the Murchison A sample (control) and the x-ray–imaged Murchison B sample. A total of 96 individual soluble organic molecules were quantified in the Murchison extracts above detection limits and included the following: 10 protein amino acids, 15 amines, six alcohols, six carbonyl compounds (five aldehydes and one ketone), 18 carboxylic acids, five hydroxy acids, four PAHs, four pentose sugars, and 28 N-heterocycles (Tables 1–9). A list of chemical structures and names of representative molecules from each compound class studied in this investigation is given as an appendix in the Supporting Information.

A comparison of the total abundances of each organic compound class (determined as the sum of the individual organic molecules quantified) in the Murchison A and B extracts is shown in Figure 3. Except for the alcohols, the total abundances of the other soluble organic compound classes were all higher (3%–3300%) in Murchison B than in Murchison A. The considerably large increase by ~3300% in the total abundance of the pentose sugars measured in Murchison B compared to Murchison A was most likely the result of analytical issues with the Murchison A sugar analyses (discussed in more detail in the Abundance and Relative Distribution of Sugars and N-Heterocycles section). If x-ray exposure during the XCT experiment had resulted in substantive molecular damage of the soluble organics in Murchison B by radiolysis, we should have observed an opposite trend, with lower total soluble organic abundances in Murchison B compared to Murchison A. If x-ray exposure had resulted in the breakdown of larger organic species such as IOM into the analytes of this study, then we would not expect to see increases in all compound classes. Instead, the most stable (e.g., PAHs) and least stable (e.g., aldehydes) compound classes both were more abundant in Murchison B. Furthermore, there were no concomitant changes to the IOM (Cody et al., 2023; Glavin et al., 2023).

To evaluate whether x-ray exposure had any measurable impact on the distributions of soluble organic compounds in the Murchison B sample, we also compared the relative abundances of individual soluble organics in each compound class extracted from the Murchison A and B samples. In the following sections, we will discuss the results from the soluble organic analyses of the Murchison A and B extracts and compare them to previously published data from different Murchison meteorite fragments.

Abundance and Distribution of Protein Amino Acids and Amines

Typical liquid chromatography UV fluorescence chromatograms of the AccQ·Tag derivatives of the C_2 to C_6 amino acids and C_1 to C_6 amine derivatives in the room temperature water extracts (sonication for 1 h) of the Murchison A and B samples are shown in Figures S3 and S4, respectively. Peaks in these chromatograms were only identified and quantified as amino acids or amines if the retention times of the UV fluorescence peaks coincided with the corresponding QqQ-MS mass peaks and expected multiple reaction monitoring (MRM) transitions of the AccQ·Tag derivatives of the standards (Tables S2 and S3). Ten protein amino acids were detected above background in the Murchison A and B extracts—asparagine, serine, glycine, aspartic acid, glutamic acid, threonine, alanine, proline, valine, and leucine—with abundances ranging from 0.04 to 23.1 nmol g^{-1} (Table 1).

Other common protein amino acids, including histidine, glutamine, arginine, cysteine, tyrosine, lysine, methionine, isoleucine, phenylalanine, and tryptophan, were not identified in the Murchison extracts above the 0.1 nmol g^{-1} level (Table 1). Several peaks in the Murchison A and B chromatograms corresponding to the non-protein amino acids β-alanine; α-, β-, and γ-amino-*n*-butyric acid; α-aminoisobutyric acid; and isovaline were also detected (Figure S3) but were not quantified in this study. These and other free non-protein amino acids were previously measured in Murchison in the

TABLE 1. Average blank-corrected free abundances (nmol g^{-1}) of the standard protein amino acids in the room temperature water extracts after sonication for 1 h of the Murchison A (control) and Murchison B (XCT) samples.

Peak #	Protein amino acids	Murchison A[a] 0.5 g extract 21.6 m^2 g^{-1}	Murchison B[a] 0.5 g extract 22.8 m^2 g^{-1}	Murchison[b] 0.5 g extract
1	Histidine	<0.1	<0.1	n.r.
2	Asparagine	0.19 ± 0.01	0.30 ± 0.03	n.r.
3	Glutamine	<0.1	<0.1	n.r.
4	Serine	0.47 ± 0.04	1.39 ± 0.22	0.37 ± 0.01
5	Arginine	<0.1	<0.1	n.r.
6	Glycine	23.10 ± 0.53	19.65 ± 0.56	21.91 ± 3.58
7	Aspartic acid	0.53 ± 0.05	0.99 ± 0.08	0.57 ± 0.08
8	Glutamic acid	0.67 ± 0.08	1.11 ± 0.06	0.66 ± 0.08
9	Threonine	0.57 ± 0.08	1.44 ± 0.08	0.12 ± 0.08
10	Alanine	2.10 ± 0.28	4.30 ± 0.21	4.67 ± 0.28
11	Proline	3.39 ± 0.46	6.57 ± 0.25	n.r.
12	Cysteine	<0.1	<0.1	n.r.
13	Tyrosine	<0.1	0.04 ± 0.01	n.r.
14	Lysine	<0.1	<0.1	n.r.
15	Methionine	<0.1	<0.1	n.r.
16	Valine	1.85 ± 0.24	3.69 ± 0.15	0.96 ± 0.12
17	Leucine	0.14 ± 0.03	0.41 ± 0.03	n.r.
18	Isoleucine	<0.1	<0.1	n.r.
19	Phenylalanine	<0.1	<0.1	n.r.
20	Tryptophan	<0.1	<0.1	n.r.
	Total sum (nmol g^{-1})	33.0 ± 0.8	39.9 ± 0.7	29.3 ± 3.6

Note: Peak numbers for Murchison A and B correspond to those shown in Figure S3. The free amino acid abundance data from a previous analysis of Murchison are shown for comparison. Extracted sample mass (g) and average specific surface area (m^2 g^{-1}) of the residue shown below the sample name.

Abbreviation: n.r., not reported.

[a]Room temperature water extracts after sonication for 1 h were analyzed by AccQ·Tag derivatization (10 min) and LC-FD/QqQ-MS. The reported uncertainties (δx) in the individual amino acid concentrations are based on the standard deviation of the average value of nine separate measurements (n) with a standard error $\delta x = \sigma_x \cdot (n)^{-1/2}$. The absolute error in the total sum was determined by adding the absolute errors of the individual compounds in quadrature.

[b]Hot water (100°C for 24 h) extract of a Murchison sample (Field Museum of Natural History, Chicago) analyzed by *o*-phthaldialdehyde/N-acetyl-L-cysteine (OPA/NAC) derivatization (15 min) and liquid chromatography with UV fluorescence and time-of-flight mass spectrometry (LC-FD/ToF-MS) detection (Friedrich et al., 2019).

Friedrich et al.'s XCT study from 2019, and their abundances did not change after x-ray exposures up to 2.8 kGy. Although we were not able to determine the abundances of the individual enantiomers of the chiral protein amino acids in Murchison, which are not separable using the AccQ·Tag derivatization method, earlier studies have already shown that x-ray exposure during XCT does not lead to statistically significant changes in the enantiomeric ratios of chiral amino acids in Murchison (Friedrich et al., 2016, 2019).

The abundance and relative distribution of the protein amino acids in the Murchison A and B room temperature water extracts were similar to the free amino acid data previously reported in hot water extracts of Murchison (Friedrich et al., 2019; Glavin et al., 2021). Interestingly, the identification of asparagine in both the Murchison A and B room temperature water extracts above blank levels (Table 1) is the first report of this protein amino acid in Murchison (Glavin et al., 2020). Given that asparagine is not very stable in water at elevated temperatures and will undergo deamidation to succinimide followed by hydrolysis to aspartic acid and isoaspartic acid with rates that are dependent on the temperature and pH (Kato et al., 2020; Pace et al., 2013), it is possible that any asparagine present in Murchison in previous studies decomposed during the standard hot water extraction procedure (100°C for 24 h) used to extract amino acids from meteorites before analysis (Glavin et al., 2011).

The total abundance of free protein amino acids in the Murchison B extract (39.9 ± 0.8 nmol g^{-1}) was ~21% higher than Murchison A (33.0 ± 0.7 nmol g^{-1}), a statistically significant difference that may be attributed to amino acid extraction efficiencies from the Murchison particles given the slightly elevated average specific surface area of 22.8 ± 0.4 m^2 g^{-1} for the Murchison B residue compared to 21.6 ± 0.3 m^2 g^{-1} for Murchison A

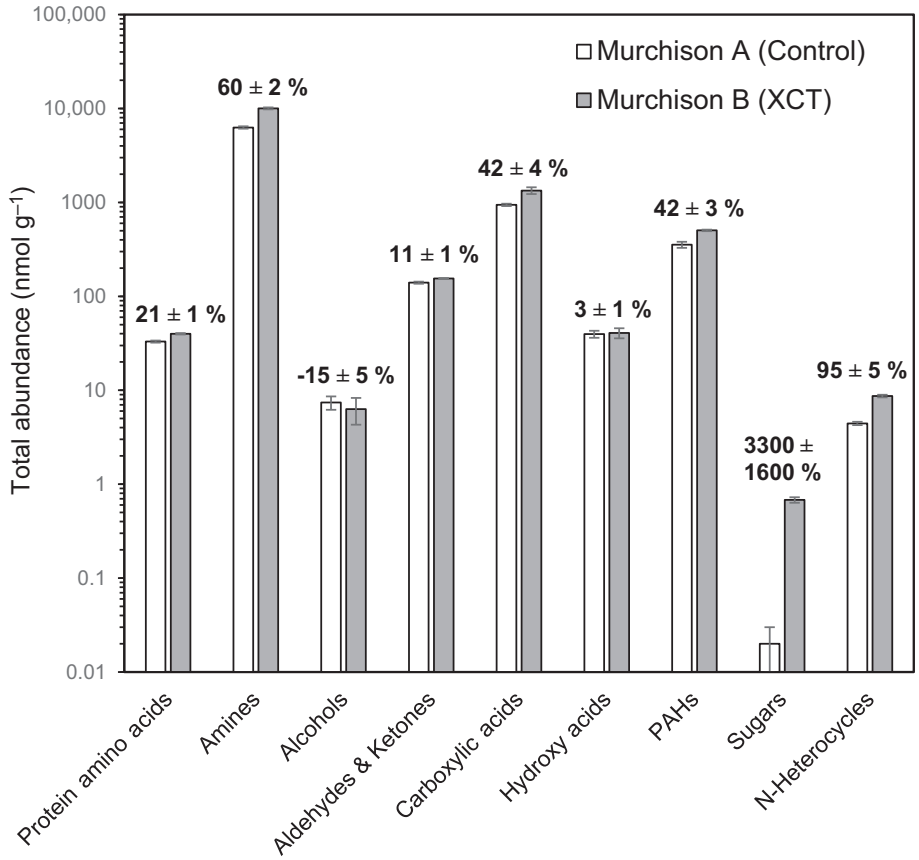

FIGURE 3. Total abundances (nmol g^{-1}) of soluble organic compounds, shown in log scale, representing the sum of the individual molecule abundances quantified in each compound class in the Murchison A (control) and Murchison B (XCT) extracts. The values at the top of the bars indicate the percent difference in total abundances in Murchison B relative to Murchison A, with uncertainties determined by standard propagation of the errors in the total abundances.

(Tables 1 and S1). The relationship between particle surface area and the abundance of extractable soluble organic compounds has long been observed in natural samples (Bergameschi et al., 1996). It should be noted that the measured specific surface areas of the Murchison A and B samples before extraction may have been lower than the values measured of the solid residues after water extraction due to agitation and fragmentation of the particles during sonication. Specific surface area measurements of the Murchison meteorite sample sets prior to extraction would be warranted before using this parameter to normalize the soluble organic abundances in the meteorite extracts.

Given the limited amount of Murchison meteorite available for this study and the mass required to enable the investigation of multiple soluble organic compound classes in the Murchison powders using different extraction and analytical techniques, we did not have sufficient sample to make replicate extractions of individual powdered aliquots of the Murchison A control sample to establish the inter-sample variability of the total soluble organic compound abundances in different portions of the meteorite. Previous analyses of amino acids in extracts from different aliquots of the same crushed Murchison meteorite sample have not shown statistically significant differences (within 1σ errors) in the total abundances (Friedrich et al., 2016; Glavin et al., 2011), although variability as high as a factor of 2 in the total abundances of some individual amino acids extracted from different Murchison meteorite fragments has been observed (Friedrich et al., 2019; Glavin et al., 2011, 2021; Simkus, Aponte, Elsila, Parker, et al., 2019). In contrast to this study, specific surface area measurements of Murchison were not made in these previous studies; therefore, the effect of particle size heterogeneity on the extraction yields and measured amino acid abundances in different aliquots of the same powdered Murchison sample could not be assessed.

Except for glycine, which, in contrast to the other protein amino acids, had a slightly lower abundance in Murchison B (19.7 ± 0.6 nmol g^{-1}) compared to Murchison A (23.1 ± 0.5 nmol g^{-1}), the relative abundances of all

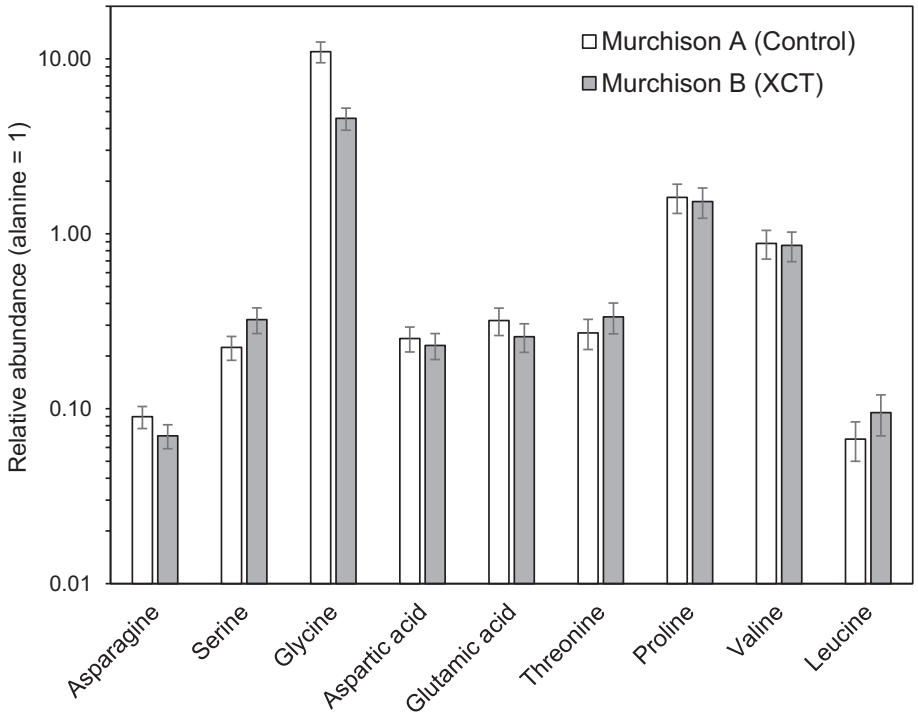

FIGURE 4. Relative abundances (alanine = 1), shown in log scale, of the protein amino acids detected above blank levels in the room temperature water extracts of Murchison A (control) and Murchison B (XCT). The uncertainties in the relative abundances were calculated by standard error propagation of the absolute errors in Table 1.

other protein amino acids between Murchison A and B were similar within analytical error (Figure 4). These results indicate that x-ray exposure of the Murchison B sample did not have any measurable impact on the relative distribution of most of the protein amino acids in the Murchison meteorite. This observation is also consistent with previous amino acid measurements of XCT-scanned Murchison samples that showed no change in the absolute or relative free amino acid abundances when compared to a Murchison control sample that was not exposed to x-rays (Friedrich et al., 2016, 2019).

In fact, no measurable free glycine decomposition was observed in any of the hot water extracts of three separate Murchison sample aliquots in a previous study after exposure to increasing x-ray doses up to 2.8 kGy (Friedrich et al., 2019). Moreover, the free glycine abundance (~22 nmol g^{-1}) measured in the Murchison extracts in the Friedrich et al. (2019) experiments was identical within error to the abundances of free glycine in the Murchison A and B samples from this study (Table 1). Based on these results, it is more likely that the lower abundance of glycine measured in Murchison B compared to Murchison A (Table 1, Figure 4) is due to chemical heterogeneity in the samples and/or measurement variability between instrument runs, rather than preferential degradation of glycine in the Murchison B sample from x-rays.

In addition to the 10 protein amino acids, 15 different amines were also identified by LC-FD/QqQ-MS (Figure S4) in the Murchison A and B room temperature water extracts—methylamine, ethylamine, isopropylamine, propylamine, *sec*-butylamine, isobutylamine, *n*-butylamine, *tert*-butylamine, 3-aminopentane, 2-amino-3-methy lbutane, *sec*-pentylamine, 2-methylbutylamine, *tert*-penty lamine, isopentylamine, and *n*-pentylamine—with abundances ranging from ~0.1 to 5000 nmol g^{-1} (Table 2). The total abundance of free amines in the Murchison B extract (10,041 ± 244 nmol g^{-1}) was 60% higher than in Murchison A (6275 ± 185 nmol g^{-1}) and, like the free protein amino acids, may also be explained by amine extraction yield differences due to the higher specific surface area of the Murchison B residue compared to the Murchison A residue (Table 2).

Moreover, the larger total increase in amine abundances of 60% in Murchison B (Figure 3) compared to a 21% increase in protein amino acids in Murchison B (Figure 3) could be explained by amine and amino acid solubility differences in water. For example, the solubility of methylamine in water at 25°C is ~108 g methylamine in 100 mL water (Schweizer et al., 1978), which is over four times higher than the solubility of glycine in water at 25°C of ~25 g in 100 mL (Budavari et al., 1996). Therefore, methylamine and other low molecular weight amines in Murchison would be expected to have higher extraction

TABLE 2. Average blank-corrected free abundances (nmol g^{-1}) of amines in the water extracts of the Murchison A (control) and Murchison B (XCT) samples after sonication at room temperature.

Peak #	Amines	Murchison A[a] 0.5 g extract 21.6 m^2 g^{-1}	Murchison B[a] 0.5 g extract 22.8 m^2 g^{-1}	Murchison[b] 0.08 g extract
1	Methylamine	2886 ± 147	5001 ± 182	228.3 ± 0.7
2	Ethylamine	467.3 ± 23.3	749.5 ± 27.6	27.5 ± 0.1
3	Isopropylamine	752.8 ± 42.6	1069 ± 55	3.60 ± 0.02
4	Propylamine	189.0 ± 10.8	248.7 ± 13.9	2.28 ± 0.02
5	*sec*-Butylamine	12.91 ± 0.74	12.63 ± 0.76	0.15 ± 0.02
6	Isobutylamine	98.8 ± 6.3	149.6 ± 9.1	1.02 ± 0.01
7	*n*-Butylamine	38.2 ± 2.8	57.8 ± 4.5	0.33 ± 0.22
8	*tert*-Butylamine	16.2 ± 1.2	21.0 ± 1.6	
9	3-Aminopentane	99.8 ± 7.0	145.1 ± 9.7	0.38 ± 0.01
10	2-Amino-3-methylbutane	1124 ± 91	1619 ± 133	1.07 ± 0.03
11	*sec*-Pentylamine	524.8 ± 42.1	816.5 ± 67.0	0.74 ± 0.01
12	2-Methylbutylamine	59.3 ± 4.2	147.3 ± 11.9	0.22 ± 0.01
13	*tert*-Pentylamine	5.55 ± 0.46	3.97 ± 0.33	<0.01
14	Isopentylamine	0.21 ± 0.02	0.12 ± 0.01	0.07 ± 0.01
15	*n*-Pentylamine	0.28 ± 0.02	0.18 ± 0.02	0.06 ± 0.01
16	*n*-Hexylamine	<0.01	<0.01	<0.01
	Total sum (nmol g^{-1})	6275 ± 185	10,041 ± 244	266 ± 1

Note: Peak numbers for Murchison A and B correspond to those shown in Figure S4. The amine abundance data from a previous analysis of Murchison is shown for comparison. Extracted sample mass (g) and average specific surface area of the residue (m^2 g^{-1}) given under the sample name.
[a]Room temperature water extracts after sonication for 1 h were analyzed by AccQ·Tag derivatization (10 min) and LC-FD/QqQ-MS. The reported uncertainties (δx) in the individual amine abundances are based on the standard deviation of the average value of nine separate measurements (n) with a standard error $\delta x = \sigma_x \cdot (n)^{-1/2}$. The absolute error in the total sum was determined by adding the absolute errors of the individual compounds in quadrature.
[b]Hot water (100°C for 24 h) extract of a Murchison sample (Field Museum of Natural History, Chicago) analyzed by AccQ·Tag derivatization (10 min) and LC-FD/Q-ToF-MS (Aponte, Elsila, et al., 2020).

yields in water compared to amino acids under the same conditions, as observed in this experiment.

Although the absolute amine abundances in the Murchison B extracts were higher than in Murchison A, we did not observe any difference in the individual amine relative abundances (methylamine = 1) in the Murchison A and B extracts outside of analytical uncertainty (Figure 5). This finding indicates that the XCT experiment did not alter the relative distribution of the amines in the Murchison meteorite, which is extremely important because the relative abundances of amines, amino acids, and other soluble organic compounds (rather than their total abundances) can be used to help constrain their origins and formation mechanisms in meteorites, including assessments of the degree of terrestrial contamination (Elsila et al., 2016; Glavin et al., 2018).

Surprisingly, the total abundances of free amines in the Murchison A and B room temperature water extracts were significantly higher (20–40 times) than the amine abundance previously measured in a hot water extract of Murchison (Aponte, McLain, et al., 2020). Because the protein amino acid abundances from the same Murchison A and B room temperature water extracts used for the amine analyses in this study were essentially identical to previously published Murchison free amino acid data (Table 1), chemical heterogeneity between meteorite samples is not a credible explanation for the elevated amine abundances measured in the Murchison A and B water extracts compared to previous Murchison amine data (Aponte, McLain, et al., 2020). Additional experiments will be required to better explain the much higher amine yield in the room temperature water extracts with sonication compared to hot water extracts.

Abundance and Relative Distribution of Carboxylic and Hydroxy Acids and Carbonyl Compounds

The GC-QqQ-MS chromatograms of representative injections of derivatized carboxylic acids, hydroxy acids, and carbonyls (aldehydes and ketones) taken from the same 100°C water extracts of the Murchison A and B samples and the procedural blank, and standards analyzed on the same day as the samples, are shown in the Supporting Information (Figures S5–S7). A total of 16 monocarboxylic and two dicarboxylic acids were detected in the Murchison A and B water extracts, with blank-corrected abundances ranging from ~3 to 619 nmol g^{-1} (Table 3). The total abundance of carboxylic acids

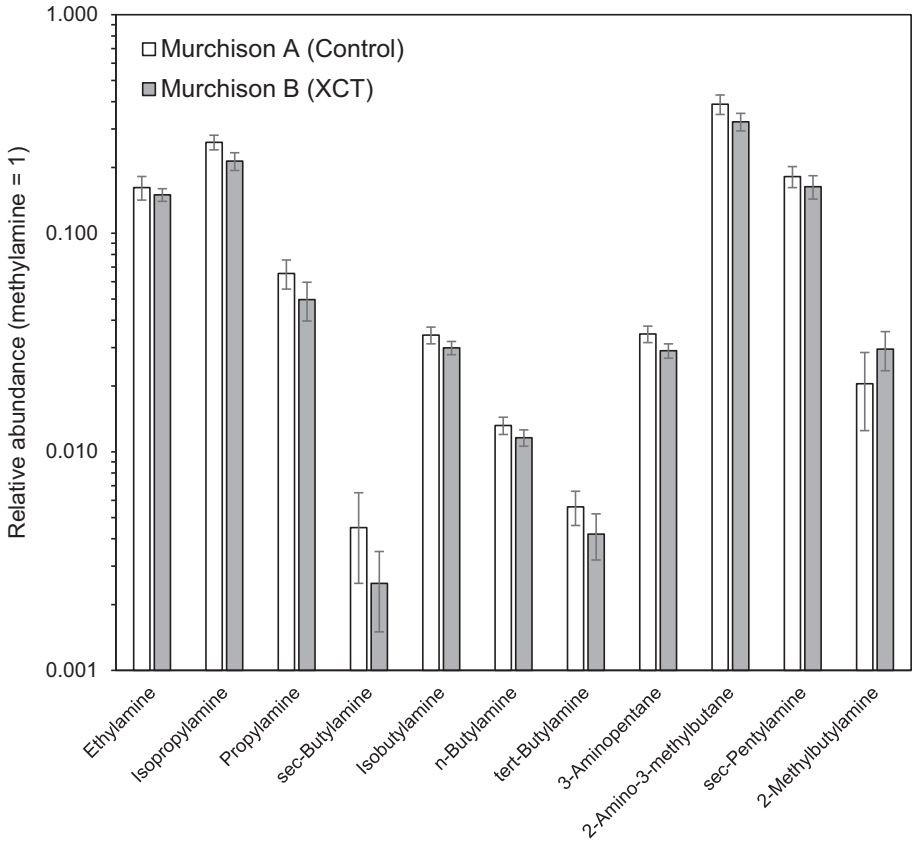

FIGURE 5. Relative abundances (methylamine = 1), shown in log scale, of the amines detected above blank levels in the room temperature water extracts of Murchison A (control) and Murchison B (XCT). The uncertainties were calculated by standard propagation of the absolute errors in Table 2.

quantified in Murchison B (1338 ± 109 nmol g^{-1}) was 42% higher (Figure 3) than the total abundance of the same carboxylic acids extracted from Murchison A (943 ± 27 nmol g^{-1}). Although specific surface area measurements of the Murchison A and B residues after hot water extraction were not performed in this study (these residues were digested in hot sulfuric acid for the analyses of cyanides), it is possible that the specific surface area of the Murchison B sample used for the carboxylic acid analyses was higher than Murchison A, which could explain the difference in carboxylic acid yields from these samples.

The abundances of the monocarboxylic and dicarboxylic acids in the Murchison A and B extracts relative to formic acid were identical within analytical uncertainties (Figure 6). Similar patterns were also obtained when plotting the distributions relative to other carboxylic acids. These data strongly suggest that exposure of Murchison B to x-rays during the XCT experiment had no effect on the relative abundances of carboxylic acids in this Murchison sample. However, we did observe significant differences in abundance and distribution of carboxylic acids in the Murchison A and B water extracts compared to a previous analysis of a different Murchison fragment (Aponte, McLain, et al., 2020), which had a total abundance of carboxylic acids that were up to approximately eight times higher than the Murchison samples analyzed in this study (Table 3). In addition, two dicarboxylic acids (succinic acid and fumaric acid) that had been previously identified in Murchison (Aponte, McLain, et al., 2020) were not detected in the Murchison A and B extracts above the 0.1 nmol g^{-1} level (Table 3). These differences may be explained by a combination of meteorite chemical or particle size heterogeneity between samples of the Murchison meteorite.

Five different hydroxy acids were identified in the Murchison A and B extracts—2-hydroxyisobutyric acid, *S*- and *R*-lactic acid, glycolic acid, (*S*,*R*)-2-hydroxybutyric acid, and *S*- and *R*-2-hydroxy-2-methylbutyric acid—with abundances ranging from 2.0 to 9.7 nmol g^{-1} (Table 4). The total abundance of these hydroxy acids in Murchison B was only ~3% higher than in Murchison A, in contrast to the carboxylic acids, which showed a much larger difference in total abundances between Murchison A and B (Figure 3). As with the amino acids and amines, it is possible that this difference could also be explained by

TABLE 3. Average blank-corrected concentrations (nmol g^{-1}) of the carboxylic acids in the hot water extracts of the Murchison A (control) and Murchison B (XCT) samples.

Peak #	Carboxylic acids	Murchison A[a] 0.5 g extract	Murchison B[a] 0.5 g extract	Murchison[b] 0.08 g extract
1	Formic acid	226.7 ± 7.8	320.2 ± 51.4	3383 ± 549
2	Acetic acid	458.5 ± 22.4	619.2 ± 85.3	3368 ± 541
3	Propanoic acid	67.5 ± 4.6	104.4 ± 22.2	313.1 ± 52.2
4	Isobutyric acid	13.9 ± 0.7	19.9 ± 3.2	61.4 ± 11.1
5	2,2,-Dimethylpropanoic acid	44.2 ± 3.1	62.2 ± 13.1	13.0 ± 2.1
6	Butyric acid	12.1 ± 0.6	18.1 ± 2.6	113.7 ± 20.2
7	2-Methylbutyric acid	6.2 ± 0.2	8.4 ± 0.7	18.4 ± 2.4
8	Isopentanoic acid	5.6 ± 0.1	7.5 ± 0.7	20.2 ± 3.8
9	2,2-Dimethylbutyric acid	4.2 ± 0.1	4.8 ± 0.2	2.6 ± 0.5
10	3,3-Dimethylbutyric acid	3.9 ± 0.1	4.3 ± 0.1	8.5 ± 5.7
11	Pentanoic acid	5.2 ± 0.2	7.0 ± 0.6	29.9 ± 6.0
12	2-Ethylbutyric/2-Methylpentanoic acid	4.0 ± 0.1	4.8 ± 0.2	<0.01
13	3-Methylpentanoic acid	3.9 ± 0.1	4.8 ± 0.2	11.6 ± 1.7
14	4-Methylpentanoic acid	3.2 ± 0.1	3.9 ± 0.2	7.8 ± 0.8
15	Hexanoic acid	4.0 ± 0.1	5.3 ± 0.4	19.3 ± 4.7
16	Benzoic acid	9.4 ± 4.6	7.4 ± 0.5	109.4 ± 35.4
17	Malonic acid	66.5 ± 11.0	130.7 ± 36.8	173.7 ± 36.1
18	Succinic acid	<0.1	<0.1	287.1 ± 64.7
19	Fumaric acid	<0.1	<0.1	62.7 ± 16.5
20	Glutaric acid	4.2 ± 0.1	5.4 ± 0.5	n.r.
	Total sum (nmol g^{-1})	943 ± 27	1338 ± 109	8003 ± 777

Note: Peak numbers for Murchison A and B correspond to those shown in Figure S5. The carboxylic acid data from a previous analysis of Murchison are shown for comparison. Extracted sample mass given under the sample name. Specific surface area data were not collected for these residues.
Abbreviation: n.d., not reported.
[a]Hot water extracts (100°C for 24 h) were analyzed after 2-pentanol derivatization using GC-QqQ-MS. The reported uncertainties (δx) in the individual carboxylic acid abundances are based on the standard deviation of the average value of three separate measurements (n) with a standard error $\delta x = \sigma_x \cdot (n)^{-1/2}$. The absolute error in the total sum was determined by adding the absolute errors of the individual compounds in quadrature.
[b]Hot water (100°C for 24 h) extract of a Murchison sample (Field Museum of Natural History, Chicago) analyzed after 2-pentanol derivatization and GC-QqQ-MS analysis (Aponte, McLain, et al., 2020).

solubility differences between carboxylic acids and hydroxy acids in water. The total abundances of the hydroxy acids in the Murchison A and B extracts (~40 nmol g^{-1}, Table 4) were approximately five times lower than the total abundance of the same hydroxy acids measured previously in a different Murchison meteorite extract (Pizzarello et al., 2010).

As with the carboxylic acids, the differences in hydroxy acid abundances in Murchison between these two studies could also be explained by meteorite chemical or particle size heterogeneity, as well as differences in the extraction or derivatization efficiencies. We did not observe any difference in the abundances of the hydroxy acids relative to glycolic acid in the Murchison A and B extracts outside of analytical uncertainties (Figure 7). Based on the abundance data shown in Table 4, there was no measurable difference outside of error in the enantiomeric ratio (S/R) of lactic acid in Murchison A (S/R = 0.9 ± 0.1) and Murchison B (S/R = 0.8 ± 0.1). The enantiomeric ratio of 2-hydroxy-2-methylbutryic acid in Murchison A and B was also ~0.8 to 0.9 (Table 4), although the uncertainty in the ratio was much higher than for lactic acid. Nevertheless, these results indicate that the XCT measurement of Murchison did not change the hydroxy acid relative abundances or the enantiomeric ratio of lactic acid in the meteorite.

We identified five aldehydes—formaldehyde, acetaldehyde, propionaldehyde, butyraldehyde, and benzaldehyde—and one ketone (2-butanone) in the Murchison A and B water extracts, with abundances ranging from 3 to ~100 nmol g^{-1} (Table 5). The total abundance of these carbonyl compounds in the Murchison B extract (154.9 ± 2.7 nmol g^{-1}) was 11% higher than the total abundances in Murchison A (139.8 ± 3.5 nmol g^{-1}). These total carbonyl abundances were lower by a factor of about four than what has been reported previously in water extracts of two different Murchison samples (Aponte, McLain, et al., 2020; Simkus, Aponte, Hilts, Elsila, et al., 2019), which again could reflect differences in meteorite particle sizes or chemical heterogeneity between the Murchison samples studied. As shown in Figure 8, no differences in the relative abundances of the carbonyl

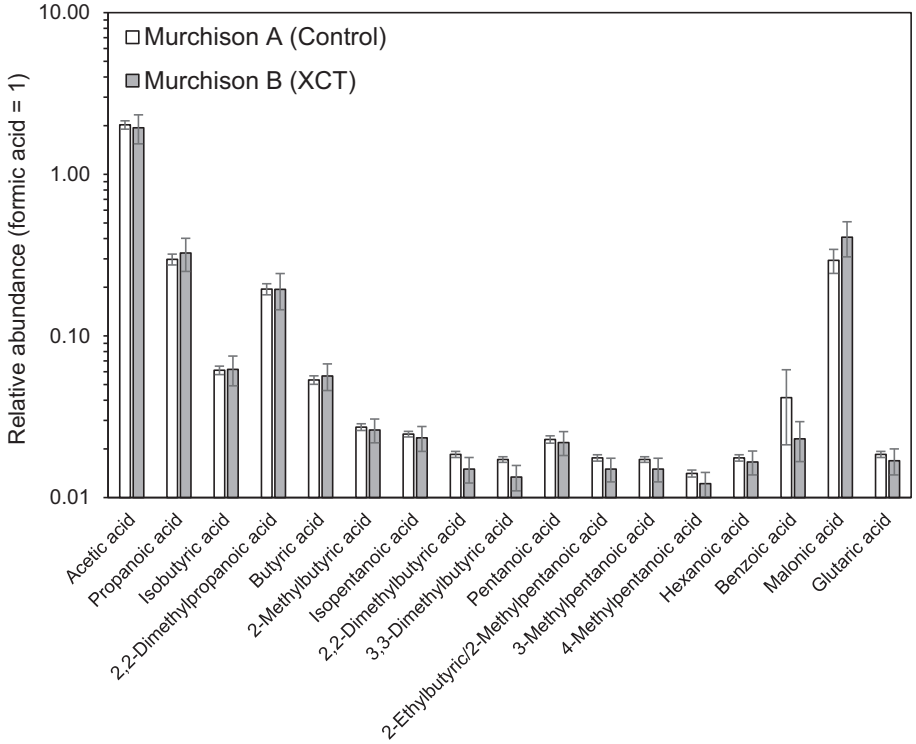

FIGURE 6. Relative abundances (formic acid = 1), shown in log scale, of the individual carboxylic acids detected above blank levels in the hot water extracts of Murchison A (control) and Murchison B (XCT). The uncertainties were calculated by standard propagation of the absolute errors in Table 3.

TABLE 4. Average blank-corrected concentrations (nmol g^{-1}) of the hydroxy acids in the hot water extracts of the Murchison A (control) and Murchison B (XCT) samples.

Peak #	Hydroxy acids	Murchison A[a] 0.5 g extract	Murchison B[a] 0.5 g extract	Murchison[b] 3 g extract
1	2-Hydroxyisobutyric acid	9.5 ± 1.8	9.1 ± 2.4	30.0 ± 1.5
2	(*S*)-Lactic acid	8.6 ± 1.1	7.7 ± 1.2	44.3 ± 2.2
3	(*R*)-Lactic acid	9.5 ± 0.5	9.7 ± 1.4	39.9 ± 2.0
4	Glycolic acid	2.3 ± 0.3	2.2 ± 0.3	65.0 ± 3.3
5	(*S*,*R*)-2-Hydroxybutyric acid	2.0 ± 0.3	2.2 ± 0.2	19.0 ± 1.0
6	(*S*)-2-Hydroxy-2-methylbutyric acid	3.5 ± 1.7	4.6 ± 3.2	6.2 ± 0.3
7	(*R*)-2-Hydroxy-2-methylbutyric acid	4.2 ± 2.0	5.2 ± 2.4	6.2 ± 0.3
	Total sum (nmol g^{-1})	39.6 ± 3.4	40.7 ± 5.0	210 ± 5

Note: The hydroxy acid abundances from a previous analysis of Murchison are shown for comparison. Peak numbers for Murchison A and B correspond to those shown in Figure S6. Total extracted mass given under the sample name. Specific surface area data were not collected for these residues.

[a]Hot water (100°C for 24 h) extracts were analyzed after 2-methylbutanol derivatization using GC-QqQ-MS. The reported uncertainties (δx) in the individual hydroxy acid abundances are based on the standard deviation of the average value of three separate measurements (n) with a standard error $\delta x = \sigma_x \cdot (n)^{-1/2}$. The absolute error in the total sum was determined by adding the absolute errors of the individual compounds in quadrature.

[b]Extracted in water at 100°C for 20 h with intermittent sonication, followed by purification of the water extracts using cation exchange chromatography, and derivatization with isobutanol and trifluoracetic anhydride for GC-MS analysis. The uncertainty in the abundances was estimated to be ±5% (Pizzarello et al., 2010).

compounds were observed in the Murchison A and B extracts, which is consistent with the carboxylic and hydroxy acids measured in the same hot water extracts and indicates that the XCT experiment did not alter the relative distributions of these soluble organics in Murchison.

Abundance and Relative Distribution of PAHs

The GC-QqQ-MS chromatograms of representative injections of the purified DCM:MeOH (9:1 v/v) extracts after sonication for 30 min at room temperature of the

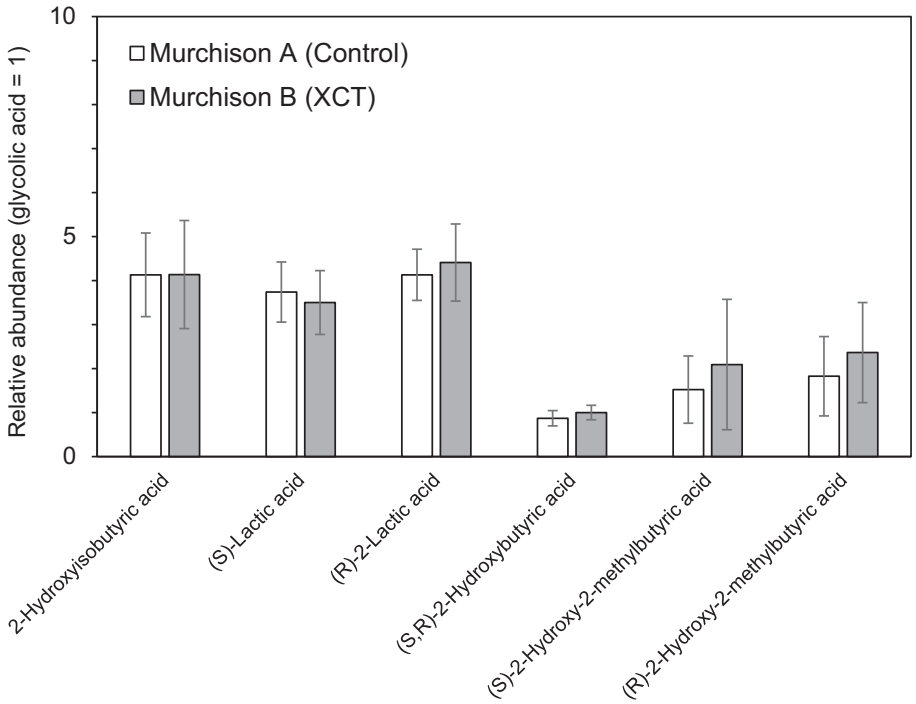

FIGURE 7. Relative abundances (glycolic acid = 1) of the individual hydroxy acids detected above blank levels in the hot water extracts of Murchison A (control) and Murchison B (XCT). The uncertainties were calculated by standard propagation of the absolute errors in Table 4.

TABLE 5. Average blank-corrected aldehyde and ketone abundances (nmol g^{-1}) in the hot water extracts of the Murchison A (control) and Murchison B (XCT) samples.

Peak #	Aldehydes and ketones	Murchison A[a] 0.5 g extract	Murchison B[a] 0.5 g extract	Murchison[b] 0.51 g extract
1	Formaldehyde	8.1 ± 2.3	6.9 ± 1.4	19.2 ± 2.8
2, 3	Acetaldehyde (*E*- and *Z*-isomers)	86.8 ± 2.5	99.7 ± 1.8	273.4 ± 48.7
4	Acetone	n.d.	n.d.	87.5 ± 15.4
5, 6	Propionaldehyde (*E*- and *Z*-isomers)	13.5 ± 0.3	15.7 ± 0.3	149.8 ± 22.8
7, 8	2-Butanone (*E*- and *Z*-isomers)	4.0 ± 0.3	5.3 ± 0.2	36.0 ± 5.7
9, 10	Butyraldehyde (*E*- and *Z*-isomers)	3.0 ± 0.2	3.4 ± 0.1	42.2 ± 6.6
11, 12	2-Pentanone (*E*- and *Z*-isomers)	n.q.	n.q.	12.3 ± 1.8
13, 14	2-Hexanone (*E*- and *Z*-isomers)	n.q.	n.q.	3.5 ± 0.9
15, 16	Benzaldehyde (*E*- and *Z*-isomers)	24.4 ± 0.9	23.9 ± 1.4	n.d.
	Total sum (nmol g^{-1})	139.8 ± 3.5	154.9 ± 2.7	623.9 ± 56.7

Note: Peak numbers for Murchison A and B correspond to those shown in Figure S7. The carbonyl compound abundances from a previous analysis of Murchison are shown for comparison. Total extracted mass given under the sample name. Specific surface area data were not collected for these residues.

Abbreviations: n.d., not detected above background levels; n.q., detected but not quantifiable due to the presence of interfering peaks.

[a]Sample hot water (100°C for 24 h) extracts were analyzed after pentafluorobenzyl hydroxylamine (PFBHA) derivatization using GC-QqQ-MS. The reported uncertainties (δx) in the individual aldehyde and ketone abundances are based on the standard deviation of the average value of three separate measurements (n) with a standard error $\delta x = \sigma_x \cdot (n)^{-1/2}$. The absolute error in the total sum was determined by adding the absolute errors of the individual compounds in quadrature.

[b]Hot water (100°C for 24 h) extract of a Murchison sample (USNM 5451,2) analyzed after PFBHA derivatization and GC–MS analysis (Simkus, Aponte, Hilts, Elsila, et al., 2019).

Murchison A and B samples and the procedural blank, and PAH standards analyzed on the same day as the samples are shown in Figure S8. No PAHs were detected in the procedural solvent blank. Several PAHs, including acenaphthene, fluoranthene, phenanthrene, and pyrene, were identified in the Murchison A and B chromatograms,

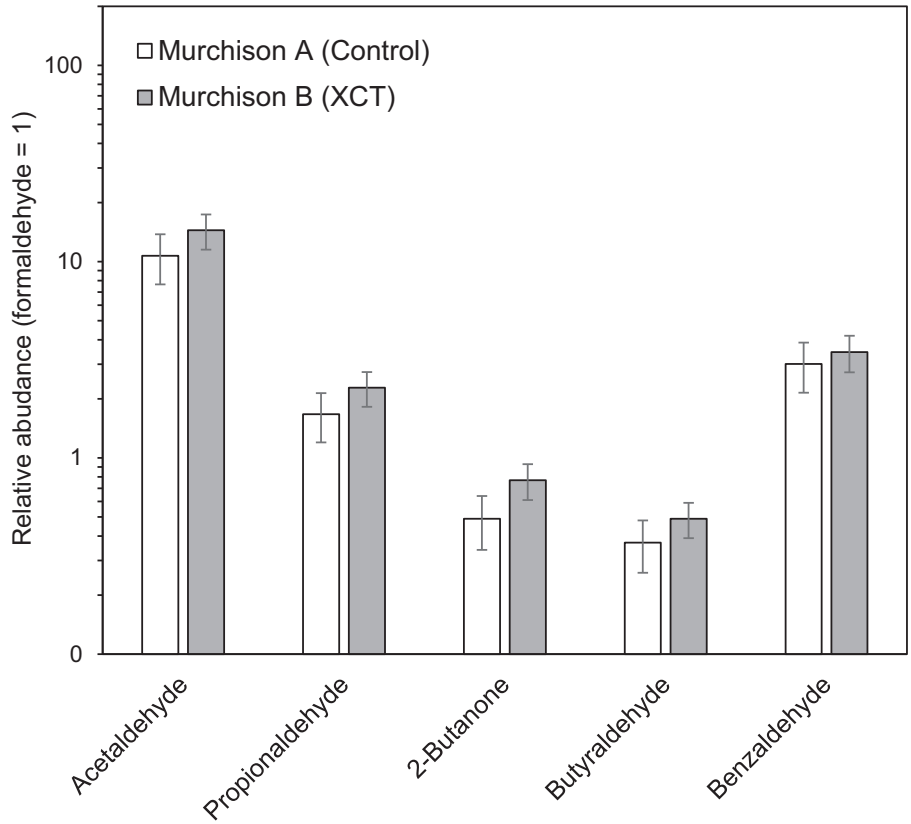

FIGURE 8. Relative abundances (formaldehyde = 1), shown in log scale, of the individual carbonyl compounds detected above blank levels in the hot water extracts of Murchison A (control) and Murchison B (XCT). The uncertainties were calculated by standard propagation of the absolute errors in Table 5.

TABLE 6. Average blank-corrected PAH abundances (nmol g^{-1}) in the room temperature DCM:MeOH extracts of the Murchison A (control) and Murchison B (XCT) samples.

Peak #	PAHs	Murchison A[a] 0.5 g extract 22.4 m^2 g^{-1}	Murchison B[a] 0.5 g extract 23.0 m^2 g^{-1}	Murchison[b] 15 g extract
1	Acenaphthene	25.0 ± 3.6	38.0 ± 6.6	37.7
2	Fluoranthene	110.0 ± 19.1	153.0 ± 2.7	24.3
3	Phenanthrene	112.0 ± 7.6	165.0 ± 5.2	27.0
4	Pyrene	108.0 ± 15.6	148.0 ± 3.9	24.3
	Total sum (nmol g^{-1})	355 ± 26	504.0 ± 9.7	113.3

Note: The PAH abundances from a previous analysis of Murchison are shown for comparison. Peak numbers in Murchison A and B correspond to those shown in Figure S8. Extracted sample mass (g) and average specific surface area of the residue (m^2 g^{-1}) given under the sample name.

[a]Sample extracts were analyzed using GC-QqQ-MS. The reported uncertainties (δx) in the individual PAH abundances are based on the standard deviation of the average value of three separate measurements (n) with a standard error $\delta x = \sigma_x \cdot (n)^{-1/2}$. The absolute error in the total sum was determined by adding the absolute errors of the individual compounds in quadrature.

[b]Murchison (Sample II) extracted by sonication at room temperature in a 9:1 by volume mixture of benzene and methanol, followed by purification using an activated silica gel column and GC–MS analysis; no uncertainties in the data were given (Kvenvolden et al., 1970; Pering & Ponnamperuma, 1971).

with abundances ranging from 25 to 165 nmol g^{-1} (Table 6). These same PAHs were previously identified in another Murchison sample (Kvenvolden et al., 1970; Pering & Ponnamperuma, 1971), although direct comparison of that data with the results from this study is challenging given the different extraction and purification methods that were used. Many other PAHs have been identified in Murchison solvent extracts (e.g., Basile et al., 1984); however, the focus of this study was on quantitative measurements of the four most abundant PAHs in the

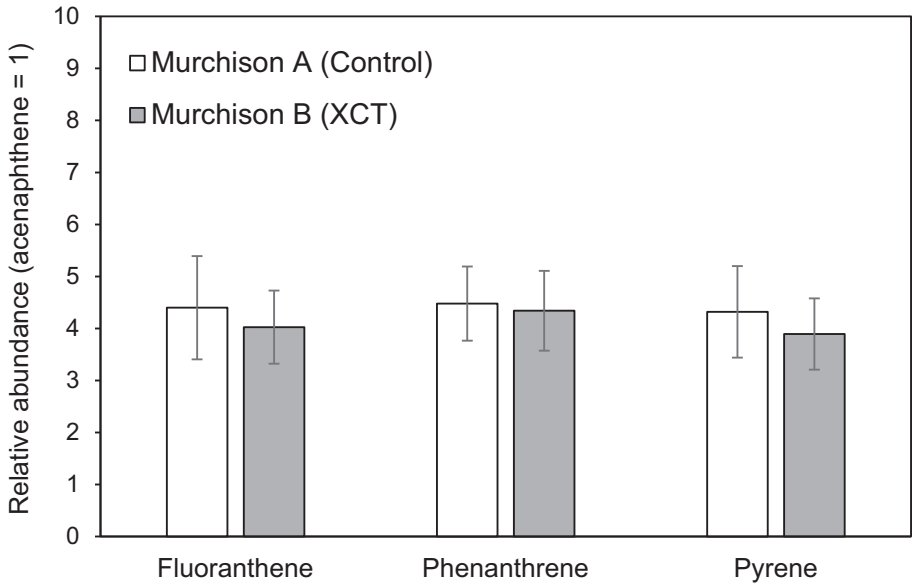

FIGURE 9. Relative abundances (acenaphthene = 1) of the PAHs quantified above blank levels in the DCM:MeOH extracts of Murchison A (control) and Murchison B (XCT). The uncertainties were calculated by standard propagation of the absolute errors in Table 6.

Murchison meteorite that typically accounts for more than 50% of the total fraction of aromatics in DCM and MeOH extracts of carbonaceous chondrites (Graham et al., 2022; Huang et al., 2015), and not a quantitative assessment of all PAHs known to be present in Murchison.

The total abundance of PAHs measured in the Murchison B extract (504.0 ± 9.7 nmol g^{-1}, Table 6) was significantly higher (42%, Figure 3) than the abundance in Murchison A (355.0 ± 26.1 nmol g^{-1}), which may simply reflect differences in the extraction yields of PAHs from the Murchison particles in the two portions based on the slightly higher average specific surface area of the Murchison B residue (23.0 ± 0.2 m^2 g^{-1}, Table S1) compared to the Murchison A residue (22.4 ± 0.3 m^2 g^{-1}, Table S1). However, because the majority of organic carbon in the Murchison meteorite is present as IOM with a chemical structure that is dominated by a network of PAH rings with cross-linking aliphatic chains (Cody et al., 2002), we cannot rule out the possibility that x-ray-induced breakdown of the IOM in the Murchison B sample during XCT resulted in the release of free soluble PAHs or other aliphatic hydrocarbons.

Future XCT experiments using only the purified IOM fraction isolated from Murchison would be required to test this hypothesis. It is also important to note that solid-state ^{1}H and ^{13}C NMR and elemental analyzer-isotope ratio mass spectrometry (EA-IRMS) data of the IOM isolated from the same Murchison A and B samples used in this study showed no evidence of changes to the total carbon, nitrogen, and hydrogen abundances or average molecular composition of the IOM because of x-ray exposure during the XCT scan (Cody et al., 2023; Glavin et al., 2023). Moreover, the relative abundances of the individual PAHs in the Murchison A and B extracts were identical within error (Figure 9), providing additional support for the hypothesis that the elevated abundances of PAHs measured in Murchison B compared to Murchison A are related to the specific surface area differences in the aliquots of sample used for the extractions rather than production from the Murchison IOM by x-rays.

Abundance and Relative Distribution of Alcohols

We were able to identify and quantify six different alcohols above procedural blank levels—methanol, ethanol, isopropanol, *n*-butanol, *n*-pentanol, and *n*-hexanol—in the Murchison A and B samples, as observed in the GC-QqQ-MS single ion chromatograms (Figure S9). The abundances of these alcohols in the DCM (50°C for 24 h) solvent extracts of Murchison A and B were low relative to the other soluble organic compounds extracted from Murchison, ranging from 0.3 to 2.5 nmol g^{-1} (Table 7).

Much higher alcohol abundances in Murchison (~14 to 156 nmol g^{-1}, Table 7) have been reported previously (Jungclaus et al., 1976). The lower alcohol abundances measured in the Murchison extracts used in this study compared to those reported by Jungclaus et al. (1976) could be due to the difference in extraction solvents (water versus DCM), extraction temperature (120°C vs. 50°C),

TABLE 7. Average blank-corrected concentrations (nmol g^{-1}) of the alcohols in the DCM extracts of the Murchison A (control) and Murchison B (XCT) samples.

Peak #	Alcohols	Murchison A[a] 0.48 g extract 13.5 m^2 g^{-1}	Murchison B[a] 0.49 g extract 9.3 m^2 g^{-1}	Murchison[b] 4.9 g extract
1	Methanol	1.2 ± 0.2	0.7 ± 0.6	156
2	Ethanol	1.7 ± 1.1	1.2 ± 1.1	65
3	Isopropanol	2.5 ± 0.4	2.1 ± 1.4	33
4	2-Methyl-2-butanol	n.d.	n.d.	n.r.
5	*tert*-Butanol	n.d.	n.d.	Tentative
6	*n*-Propanol	n.d.	n.d.	Tentative
7	(*R,S*)-*sec*-Butanol	n.d.	n.d.	n.r.
8	Isobutanol	n.d.	n.d.	n.r.
9	2,2-Dimethyl-1-propanol	n.d.	n.d.	n.r.
10	*n*-Butanol	1.2 ± 0.2	1.3 ± 0.6	14[c]
11	(*R,S*)-3-Methyl-2-butanol	n.d.	n.d.	n.r.
12	(*R,S*)-2-Pentanol	n.d.	n.d.	n.r.
13	3-Pentanol	n.d.	n.d.	n.r.
14	3-Methyl-1-butanol	n.d.	n.d.	n.r.
15	*n*-Pentanol	0.3 ± 0.1	0.4 ± 0.1	n.r.
16	2-Methyl-1-butanol	n.d.	n.d.	n.r.
17	4-Methyl-1-pentanol	n.d.	n.d.	n.r.
18	*n*-Hexanol	0.5 ± 0.1	0.6 ± 0.1	n.r.
	Total sum (nmol g^{-1})	7.4 ± 1.2	6.3 ± 2.0	268

Note: The alcohol abundances from a previous analysis of Murchison are shown for comparison. Peak numbers in Murchison A and B correspond to those shown in Figure S9. Extracted sample mass (g) and average specific surface area of the residue (m^2 g^{-1}) given under the sample name.
Abbreviations: n.d., not detected above background levels; n.r., not reported.
[a]Samples extracted in DCM (50°C for 24 h) and analyzed after (S)-(−)-N-(trifluoroacetyl)pyrrolidine-2-carbonyl chloride (S-TPC) using GC-QqQ-MS. The reported uncertainties (δx) in the individual hydroxy acid abundances are based on the standard deviation of the average value of three separate measurements (n) with a standard error $\delta x = \sigma_x \cdot (n)^{-1/2}$. The absolute error in the total sum was determined by adding the absolute errors of the individual compounds in quadrature.
[b]Sample extracted in distilled water in an evacuated and sealed ampoule and heated to 120°C for 4 days followed by GC–MS analysis of the extract; no uncertainties reported (Jungclaus et al., 1976).
[c]Reported as a sum of multiple butyl alcohol isomers (C_4H_9OH).

and/or extraction durations (96 h versus 24 h) that were used. This study is the first report of *n*-pentanol and *n*-hexanol in the Murchison meteorite (Table 7). Further optimization of the extraction procedure to improve the alcohol yields from Murchison and other meteorites is currently in progress. Although the uncertainties in the relative alcohol abundances are large, we did not observe any measurable difference in the relative distribution of the alcohols in the Murchison A and B samples (Figure 10).

The alcohols were the only soluble organic compound class in Murchison that we investigated in this study where the total abundances in Murchison A were higher than in Murchison B, although the measured difference was within analytical error (Figure 3, Table 7). The elevated total abundances of alcohols in Murchison A (7.4 ± 1.2 nmol) and, thus, higher extraction yield compared to Murchison B (6.3 ± 2.0 nmol) are consistent with the nitrogen gas adsorption measurements in Table S1 that show that the Murchison A residue had a higher average specific surface area (13.5 ± 0.1 m^2 g^{-1}) compared to Murchison B (9.3 ± 0.3 m^2 g^{-1}). Moreover, the comparatively low specific surface area values of these Murchison A and B residues relative to the Murchison residues from the amino acid/amine and PAH extractions that had specific surface areas that were approximately double (Table S1) may also help explain why the alcohol extraction yields from these Murchison sample aliquots were so much lower than the alcohol abundances in Murchison reported in the previous study. Additional experiments will be needed to better understand how the average specific surface areas of Murchison powders before and after solvent extraction correlate to the absolute yields of these soluble organic compounds in the meteorite extracts.

Abundance and Relative Distribution of Sugars and N-Heterocycles

The chromatograms from the GC–MS analyses of the pentose sugar derivatives in the water and 2% HCl room temperature extracts of Murchison A and B and the serpentine blank, as well as a pentose standard containing

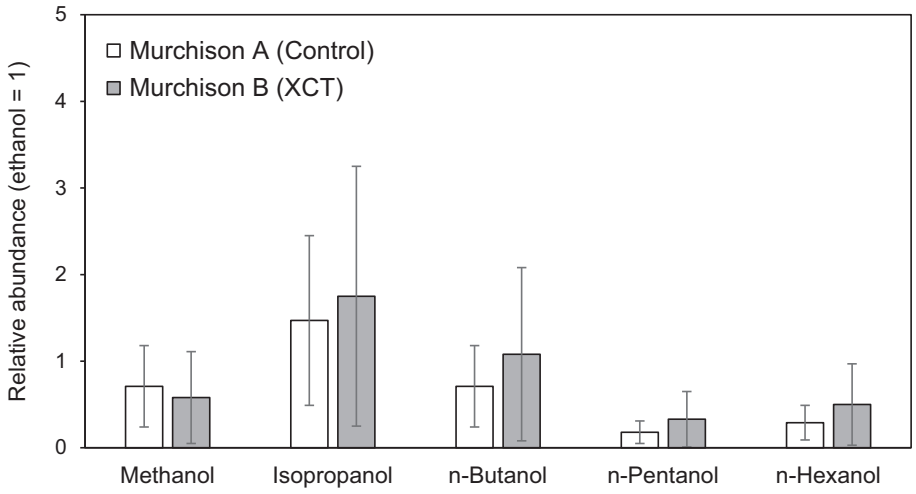

FIGURE 10. Relative abundances (ethanol = 1) of the alcohols quantified above blank levels in the DCM extracts of Murchison A (control) and Murchison B (XCT). The uncertainties were calculated by standard propagation of the absolute errors in Table 7.

TABLE 8. Average blank-corrected concentrations (nmol g^{-1}) of the pentoses in the water and 2% HCl extracts of the Murchison A (control) and Murchison B (XCT) samples after sonication at room temperature.

Peak #	Pentose sugars	Murchison A[a] 0.95 g extract	Murchison B[a] 1.01 g extract	Murchison[b] 2.0 g extract
1	Ribose	<0.02	0.05 ± 0.01	0.17 ± 0.02
2	Lyxose	<0.02	0.02 ± 0.01	0.045 ± 0.004
3	Arabinose	0.02 ± 0.02[c]	0.32 ± 0.03	0.80 ± 0.08
4	Xylose	<0.04	0.29 ± 0.03	1.20 ± 0.12
	Total sum (nmol g^{-1})	0.02 ± 0.02	0.68 ± 0.04	2.22 ± 0.15

Note: Peak numbers in Murchison A and B correspond to those shown in Figure S10. Previously published sugar abundance data from a different Murchison sample are shown for comparison. Extracted mass given under the sample name. Specific surface area data were not collected for these residues.

[a]Sample extracts were analyzed after derivatization using GC–MS. The reported uncertainties (δx) in the individual sugar abundances are based on the standard deviation of the average value of three separate measurements (n) with a standard error $\delta x = \sigma_x \cdot (n)^{-1/2}$. The absolute error in the total sum was determined by adding the absolute errors of the individual compounds in quadrature.

[b]Murchison sample (Field Museum of Natural History, Chicago) analyzed using the same extraction and analytical methods (Furukawa et al., 2019).

[c]Tentatively identified above blank levels.

ribose, lyxose, arabinose, and xylose, are shown in Figure S10. Because all four of these sugars had previously been identified in another Murchison sample extracted and analyzed using the same methods at abundances ranging from 0.05 to 1.2 nmol g^{-1} (Furukawa et al., 2019), it was surprising that arabinose was only tentatively identified in Murchison A at the 0.02 nmol g^{-1} level and the other pentoses were not identified at all in Murchison A above the 0.02–0.04 nmol g^{-1} level (Table 8). In contrast to Murchison A, all four pentoses were identified in the Murchison B extract at abundances ranging from 0.02 to ~0.3 nmol g^{-1} (Table 8).

During the extraction procedure, it was noted that the water eluate from the desalted Murchison A sample appeared to be much darker in color (orangish) compared to the Murchison B desalted extract, which was a lighter yellow. This difference in color could have been due to a higher concentration of Fe^{2+} or other metal ions in the Murchison A extract; metal ions are known to inhibit the chemical derivatization of sugars.

Therefore, it is possible that pentoses were present in the Murchison A extract but were not detected by GC-MS because the sugars did not react to form the aldononitrile acetate derivatives. Unfortunately, all the Murchison sample mass allocated for the sugar analyses was extracted, so the sugar analysis of Murchison A could not be repeated. Nevertheless, the distribution of pentose sugars in the Murchison B extract was similar to another Murchison sample that had not been exposed to x-rays during XCT (Figure 11), which gives some confidence that the pentoses in Murchison B were not significantly impacted by x-ray exposure. The Murchison A and B

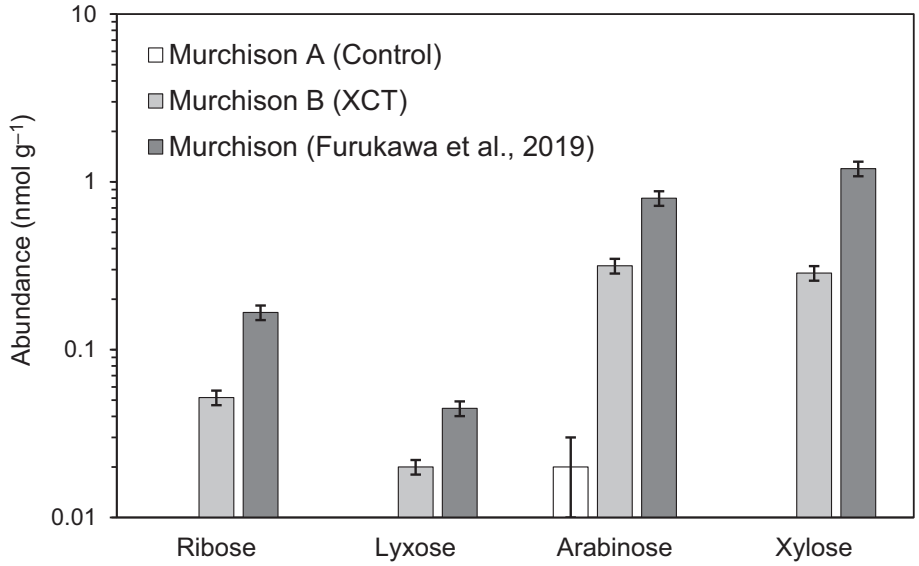

FIGURE 11. Abundances (nmol g^{-1}), shown in log scale, of the pentose sugars in the Murchison A (control) and Murchison B (XCT) room temperature water and 2% HCl extracts, compared to previous results from a fragment of a different Murchison meteorite sample provided by the Field Museum of Natural History in Chicago (Furukawa et al., 2019). The uncertainties were calculated by standard propagation of the absolute errors in Table 8. Ribose, lyxose, and xylose were not detected above background in the Murchison A extract and are therefore not shown in the plot.

residues after extraction were acid demineralized for IOM analyses; therefore, nitrogen gas adsorption measurements were not performed on these samples.

In contrast to the sugars, the N-heterocycles did not require derivatization before LC-MS analyses; therefore, the detection of these compounds should not have been significantly impacted by any differences in the metal ion concentrations of the Murchison A and B extracts. The high-resolution mass chromatograms from the LC-Orbitrap-MS analyses with individual peaks corresponding to 28 different N-heterocycles in the Murchison A and Murchison B sample extracts are shown in Figures S11 and S12. The names of the purines, pyrimidines, and other N-heterocycles identified in the Murchison extracts are given in Table 9, with abundances that ranged from ~0.001 to 1.0 nmol g^{-1}. Several N-heterocycles were identified in these Murchison samples, including 4-amino-5-hydroxypyrimidine, 4-amino-6-hydroxypyrimidine, 5,6-dimethyluracil, 5-ethyluracil, 1-methyl-1H-imidazole-2-carboxylic acid, 5-methylnic otinamide, and 2-, 4-, 5-, and 6-methylnicotinic acid, 4-methylnicotinic acid, that had not been previously reported in the Murchison meteorite (Oba et al., 2022), but were detected in interstellar ice analogs (Oba et al., 2019). The total abundance of N-heterocycles in Murchison B (8.7 ± 0.3 nmol g^{-1}) was nearly twice the total abundance of N-heterocycles in Murchison A (4.4 ± 0.2 nmol g^{-1}).

Although surface area measurements on these Murchison samples were not performed, it is possible that particle size differences or chemical heterogeneity between the two samples could explain the abundance differences. For most of the purines and pyrimidines identified in the Murchison extracts, the relative abundances in Murchison A and Murchison B were similar within error (Figure 12), indicating that the XCT experiment did not have a significant impact on the N-heterocycle distribution in Murchison. However, a few compounds, including thymine, 4-amino-5-hydroxypyrimidine, and 5-ethyluracil, did show some differences in abundances relative to adenine outside of analytical uncertainty (Figure 12). Therefore, we cannot rule out the possibility from this data set that x-rays from the XCT had some impact on these pyrimidines. Based on previous experiments, however, thymine and other pyrimidines do not decompose when exposed to total gamma ionizing radiation doses up to ~1 mGy (Hammer et al., 2019); thus, it seems highly improbable that the much lower total x-ray dose of 180 Gy used in this study led to measurable radiolytic degradation of N-heterocycles in Murchison. Of course, it is also possible that the observed differences in N-heterocycle abundances between Murchison A and B are due to chemical heterogeneity and/or extraction efficiency differences.

Nontargeted Analyses of Soluble Compounds and Their Molecular Distributions

The methanol extracts of Murchison A and B were analyzed with FTICR-MS using different complementary ionization methods: electrospray in positive ionization

TABLE 9. Summary of the average blank-corrected concentrations (nmol g^{-1}) of the N-heterocycles in the water and 2% HCl extracts of the Murchison A (control) and Murchison B (XCT) samples after sonication at room temperature.

Peak #	N-Heterocycles	Murchison A[a] 0.95 g extract	Murchison B[a] 1.01 g extract	Murchison[b] 2.0 g extract
1	Uracil	0.13 ± 0.04	0.22 ± 0.05	0.13
2	1-Methyluracil	0.014 ± 0.002	0.032 ± 0.018	0.008
3	Thymine	0.005 ± 0.001	0.160 ± 0.001	0.04
4	4-Amino-5-hydroxypyrimidine	0.018 ± 0.002	0.008 ± 0.001	n.r.
5	4-Amino-6-hydroxypyrimidine	0.001 ± 0.001	0.002 ± 0.001	n.r.
6	5,6-Dimethyluracil	n.q.	0.050 ± 0.002	n.r.
7	5-Ethyluracil	0.012 ± 0.003	0.19 ± 0.01	n.r.
8	Adenine	0.016 ± 0.008	0.029 ± 0.006	0.11
9	Hypoxanthine	0.026 ± 0.012	0.048 ± 0.007	0.18
10	Guanine	0.08 ± 0.04	0.250 ± 0.003	0.48
11	Isoguanine	0.001 ± 0.001	0.006 ± 0.001	0.003
12	Xanthine	0.058 ± 0.013	0.08 ± 0.02	0.26
13	Purine	0.0005 ± 0.0001	0.0004 ± 0.0001	0.003
14	2,6-Diaminopurine	0.0008 ± 0.0001	0.0350 ± 0.0001	0.001
15	4-Imidazolecarboxylic acid	0.90 ± 0.08	1.50 ± 0.16	0.80
16	2-Imidazolecarboxylic acid	0.39 ± 0.03	0.28 ± 0.02	0.17
17	Nicotinamide	0.02 ± 0.02	0.04 ± 0.01	0.08
18	Picolinamide	0.004 ± 0.001	0.003 ± 0.001	0.008
19	Isonicotinic acid	0.51 ± 0.06	1.23 ± 0.06	0.43
20	Nicotinic acid	0.87 ± 0.26	1.82 ± 0.04	0.74
21	1-Methyl-1H-imidazole-5-carboxylic acid	0.053 ± 0.021	0.060 ± 0.002	1.19
22	1-Methyl-1H-imidazole-2-carboxylic acid	0.096 ± 0.095	0.19 ± 0.01	n.r.
23	4-Methyl-1H-imidazole-5-carboxylic acid	0.117 ± 0.038	0.20 ± 0.04	0.21
24	5-Methylnicotinamide	n.q.	0.070 ± 0.004	n.r.
25	2-Methylnicotinic acid	0.093 ± 0.012	0.20 ± 0.01	n.r.
26	4-Methylnicotinic acid	0.15 ± 0.03	0.42 ± 0.02	n.r.
27	6-Methylnicotinic acid	0.556 ± 0.012	0.95 ± 0.14	n.r.
28	5-Methylnicotinic acid	0.318 ± 0.066	0.61 ± 0.16	n.r.
	Total sum (nmol g^{-1})	4.44 ± 0.18	8.68 ± 0.29	4.84

Note: Peak numbers in Murchison A and B correspond to those shown in Figures S11 and S12. Previously published N-heterocycle abundance data from a different Murchison sample is shown for comparison. Extracted mass given under the sample name. Specific surface area data were not collected for these meteorite residues.

Abbreviations: n.q., not quantified due to analytical interferences; n.r., not reported.

[a]Sample extracts were analyzed using HPLC/ESI-HRMS after the cation-exchange resin treatment (Oba et al., 2022; Takano et al., 2010). The reported uncertainties (δx) in the individual N-heterocycle abundances are based on the standard deviation of the average value of two to four separate measurements (n) with a standard error $\delta x = \sigma_x \cdot (n)^{-1/2}$. The absolute error in the total sum was determined by adding the absolute errors of the individual compounds in quadrature.

[b]Data from another Murchison sample (Field Museum of Natural History, Chicago) analyzed using the same extraction and analytical methods; no errors were reported (Oba et al., 2022).

mode [ESI(+)], negative ionization mode [ESI(−)], and atmospheric pressure photoionization in positive mode [APPI(+)]. Methanol extracts obtained through soft extraction contain the widest range of organic molecules and are specifically designed to retain the original composition of these molecules (Schmitt-Kopplin et al., 2010). In our analysis with ESI(−)-FTICR-MS, a total of 8292 features could be annotated in Murchison A with molecular formulae of CH, CHN, CHS, CHO, CHNO, CHOS, and CHNOS. In comparison, 7719 features were determined for the Murchison B extract with the same molecular formulae as above. For each ionization source, the number of features and corresponding percent distribution of all chemical species were similar in Murchison A and B (Table 10). Previous studies analyzing methanol extracts of Murchison also found comparable molecular distributions with ESI(−)-FTICR-MS (Hertkorn et al., 2015; Hertzog et al., 2019).

The compositional space of Murchison A and Murchison B as measured with ESI(−)-FTICR-MS was visualized in Van Krevelen diagrams and demonstrates the chemical similarity between both meteorite extracts (Figure 13a). Plotting the intensity ratios between Murchison A and Murchison B as Int_B/Int_A revealed no

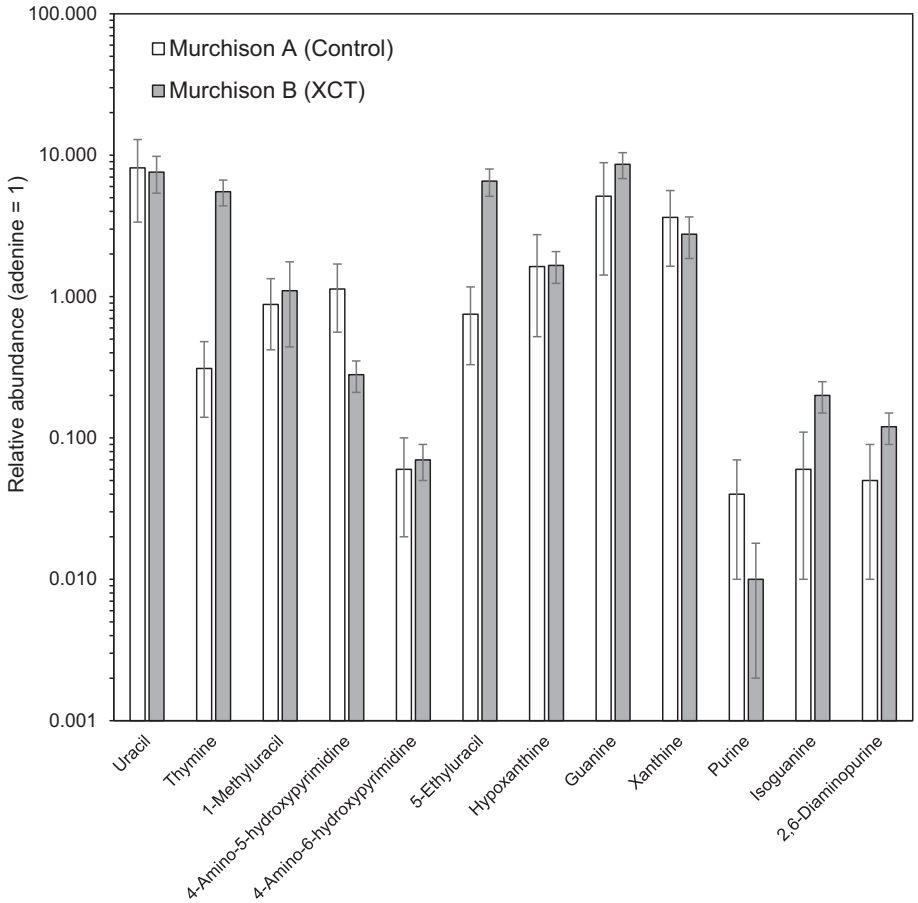

FIGURE 12. Relative abundances (adenine = 1), shown in log scale, of the pyrimidines and purines in the room temperature and 2% HCl extracts of Murchison A (control) and Murchison B (XCT). The uncertainties were calculated by standard propagation of the absolute errors in Table 9.

TABLE 10. Composition of the different heteroatom classes of soluble organic molecules in the Murchison A and Murchison B MeOH extracts analyzed by ESI(−), ESI(+), and APPI(+)-FTICR-MS with the total number of features and corresponding percentages.

	ESI(−)		ESI(+)		APPI(+)	
Class	Murchison A	Murchison B	Murchison A	Murchison B	Murchison A	Murchison B
CH	–	–	2 (0.1%)	1 (<0.1%)	198 (5.7%)	204 (5.9%)
CHN	156 (1.9%)	187 (2.4%)	597 (20.3%)	616 (20.4%)	532 (15.3%)	532 (15.3%)
CHS	7 (0.1%)	5 (0.1%)	–	1 (<0.1%)	9 (0.3%)	9 (0.3%)
CHO	1116 (13.5%)	1003 (13.0%)	273 (9.3%)	298 (9.9%)	803 (23.1%)	806 (23.3%)
CHNO	2647 (31.9%)	2452 (31.8%)	1735 (59.0%)	1855 (61.3%)	1711 (49.3%)	1697 (49.0%)
CHOS	1823 (22.0%)	1705 (22.1%)	44 (1.5%)	43 (1.4%)	115 (3.3%)	135 (3.9%)
CHNOS	2543 (30.7%)	2367 (30.7%)	292 (9.9%)	211 (7.0%)	104 (3.0%)	83 (2.4%)
Total	8292	7719	2943	3025	3472	3466

significant changes in intensities after the XCT scan, which is shown by the linearity of the intensity ratios. Using conservative calculations, over 90% of the annotated molecular formulae were identified as identical features in Murchison A and Murchison B (Figure 13b). The percentage of unique annotations for Murchison A (8.1%) and Murchison B (1.2%) was reasonably low. The higher number of unique annotations in Murchison A was primarily the result of the larger number of total annotated molecular formulae.

Considering the carbon oxidation state of chemical spaces featuring CHO, CHNO, and CHOS, the

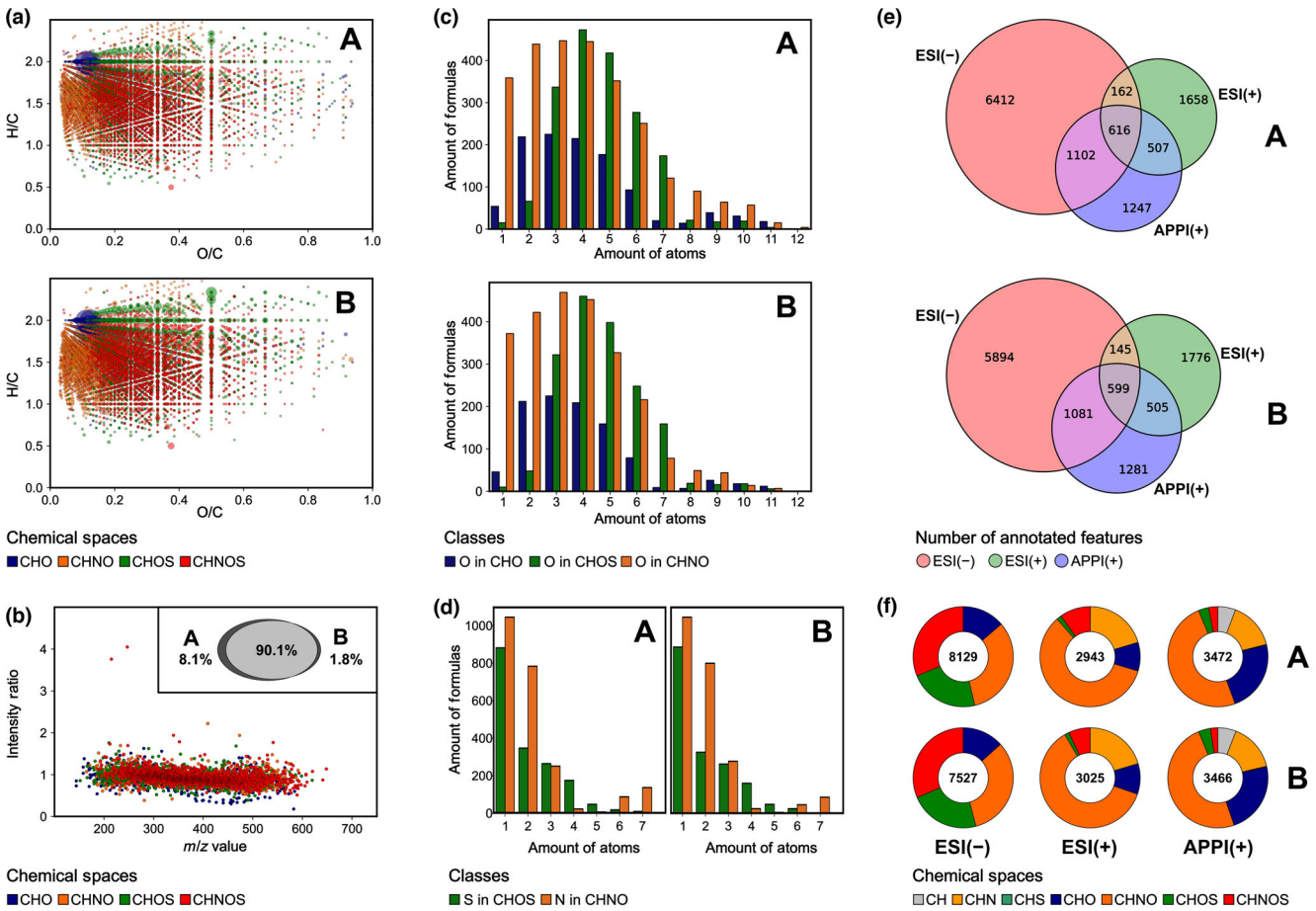

FIGURE 13. Nontargeted compositional profiling of the methanol extracts from Murchison A and B analyzed with FTICR-MS. (a–d) ESI(−) coupled to FTICR-MS. (a) Van Krevelen diagrams of annotated molecular formulae classified as CHO, CHNO, CHOS, or CHNOS. Neutral molecular formulae are also plotted. The bubble size indicates the proportional intensities of corresponding peaks in the spectra. (b) Intensity ratios (Int_B/Int_A) of identical molecular formulae annotated in Murchison A and B. Intersecting and unique annotations are displayed in a Venn diagram. (c) Oxygen frequency in CHO, CHOS, and CHNO. (d) Sulfur and nitrogen frequency in CHOS and CHNO, respectively. (e) Venn diagrams of the total annotated molecular formulae obtained from data in ESI(−), ESI(+), and APPI(+) FTICR-MS. (f) Distribution of chemical spaces for studied ionization setups.

Murchison A and Murchison B methanol extracts were highly similar (Figure 13c). Likewise, distributions for sulfur in the CHOS space and nitrogen in the CHNO space revealed only marginal differences between Murchison A and Murchison B (Figure 13d). Comparing multiple ionization features obtained with ESI(−), ESI(+), and APPI(+), it is clear that the different measurements highly depend on the detection mode and the ionization source used (see also Supporting Information, Figures S13–S15). With over 11,000 annotated features, only 616 were commonly observed with all three ionization modes for Murchison A and only 599 for Murchison B (Figure 13e). These results were consistent with previous results from Hertzog et al. (2019). The observation and visual display of the heteroatom class distributions for all ionization methods used showed negligible differences between the molecular distributions in the Murchison A and B extracts (Figure 13f).

The heteroatom class distributions observed in the hexane, DCM, and water extracts of Murchison A and B, as illustrated in the Van Krevelen diagrams, were also similar (Figure S15), confirming that any small differences observed in the solvent extracts of Murchison A and B were more likely due to charge effects rather than x-ray exposure of Murchison B during the XCT scan. Given the smaller sized portions (~40 mg) of Murchison used for these non-targeted soluble organic measurements, and the fact that the Murchison A and B samples were ground down further in a mortar as part of the solvent extraction procedure, it is unlikely that particle size heterogeneity in these samples had any significant impact on the FTICR-MS results.

SUMMARY AND CONCLUSIONS

We used the Murchison carbonaceous chondrite as an analog to determine whether XCT imaging could affect the organic composition of Bennu samples returned by OSIRIS-REx. To test this, we exposed one split of a crushed sample of Murchison to a polychromatic x-ray beam using the XCT instrument at JSC, and we used the other split as a non-irradiated control. The irradiated split was exposed to a total of ~180 Gy, representing the maximum x-ray dose that a Bennu sample would experience during XCT as part of the preliminary examination.

Using a variety of gas and liquid chromatography mass spectrometry techniques across multiple laboratories, we measured the abundance and distribution of protein amino acids, amines, carboxylic acids, hydroxy acids, carbonyl compounds, PAHs, alcohols, sugars, and N-heterocycles in solvent extracts from the irradiated and control samples. To investigate an even broader range of soluble organic species present in Murchison, we also conducted non-targeted chemical profiling measurements of both samples using FTICR-MS.

Based on the results, we conclude that the XCT imaging experiment had no measurable effect on the relative abundances of the protein amino acids, amines, alcohols, carbonyls, carboxylic and hydroxy acids, PAHs, and N-heterocycles, or the distribution of CH-, CHN-, CHS-, CHO-, CHNO-, CHOS-, and CHNOS-bearing chemical species within procedural and analytical errors. Owing to an analytical problem with the sugar analysis of the control sample, we are unable to conclude definitively whether the XCT experiment had any impact on the abundances or distribution of pentoses.

In comparing the relative distributions and total abundances of soluble organic compounds in the Murchison samples, we did not find any evidence of significant decomposition (i.e., radiolysis) by x-rays during the XCT scan. In fact, in all cases except for the alcohols, higher total abundances of soluble organic compounds were recovered from the x-ray–exposed extracts compared to the control. The correlation between the total abundances of amino acids and amines, PAHs, and alcohols in the Murchison extracts and the specific surface areas of the residues after extraction strongly suggest that the measured differences in the total soluble organic abundance are due to particle size heterogeneity and solvent extraction efficiency differences, rather than x-rays. However, we cannot completely rule out the possibility that some soluble organic compounds in the XCT-scanned extracts may have been produced from the degradation of IOM by x-rays. Additional experiments will be needed to test this hypothesis.

Our analysis of soluble organic compounds in Murchison, together with the bulk chemistry and IOM measurements made on the same samples (Cody et al., 2023; Glavin et al., 2023), provides confidence that XCT at total doses up to 180 Gy will not alter the composition of organic matter in the Bennu samples returned by the OSIRIS-REx mission, assuming they have a similar composition to carbonaceous chondrites. Based on other experiments using Murchison samples, much higher ionizing radiation exposures (on the order of megagrays) would be required to see significant degradation of the organics. Most of the total mass (~70%) of the returned sample from Bennu will be archived at JSC and not imaged by XCT while in curation. This material will therefore be available for thermoluminescence measurements and other analyses that may be sensitive to x-ray exposure.

Future sample return missions that are also planning to use XCT as a reconnaissance tool, such as Mars Sample Return (Kminek et al., 2014), need to consider the XCT exposure time and total ionizing radiation dose and conduct similar tests if needed. Because the samples that are planned to be returned from Mars are sealed inside titanium metal tubes, higher x-ray energies and doses than those used in this study may be required to image the sample cores using XCT. Future investigations to study the impact of x-rays and other forms of ionizing radiation on soluble organics in solid materials should also consider crushing smaller mass portions (~1 g) of the sample in multiple stages so that they can be more thoroughly powdered in a mortar. In addition, the crushed materials should also be sieved as part of the homogenization process to minimize particle size heterogeneity before radiation exposure.

Acknowledgments—We thank Tim McCoy, Curator of Meteorites at the Smithsonian National Museum of Natural History, for the Murchison meteorite samples used for this study and Jon Friedrich at Fordham University for assistance with the total x-ray dose calculation from the XCT experiment and for providing a helpful review of the manuscript. We also appreciate helpful comments from Hikaru Yabuta and the anonymous reviewer. This material is based on work supported by NASA under Award NNH09ZDA007O and Contract NNM10AA11C issued through the New Frontiers Program. We are grateful to the OSIRIS-REx Sample Organics Analysis Working Group for feedback on this work and the entire OSIRIS-REx Team for making the return of samples from asteroid Bennu possible. D.P.G, J.C.A., J.P.D., J.E.E., H.L.M, E.T.P., and D.N.S. also appreciate funding support from the Goddard Center for Astrobiology and a grant from

the Simons Foundation (SCOL award 302497 to J.P.D.). H.L.M. and D.N.S. appreciate support through NASA under award number 80GSFC21M0002. P.S.K. and M.L. are funded by the Deutsche Forschungsgemeinschaft (DFG, German Research Foundation): Project-ID 364653263—TRR 235 (CRC 235). H.N. is funded by the Japan Society for the Promotion of Science under KAKENHI grants JP20H00202 and JP20H05846. The data used to generate the relative abundance graphs shown in Figures 3–12 were taken from Tables 1–9. The data used to generate the plots shown in Figure 13 and Figures S3–S15 can be found in the Supporting Information (Data S1).

Conflict of Interest Statement—The authors declare no conflict of interest.

Data Availability Statement—The data that supports the findings of this study are available in the supplementary material of this article.

Editorial Handling—Dr. Josep M. Trigo-Rodríguez

REFERENCES

Aponte, J. C., Elsila, J. E., Hein, J. E., Dworkin, J. P., Glavin, D. P., McLain, H. L., Parker, E. T., Cao, T., Berger, E. L., and Burton, A. S. 2020. Analysis of Amino Acids, Hydroxy Acids, and Amines in CR Chondrites. *Meteoritics & Planetary Science* 55: 2422–39.

Aponte, J. C., McLain, H. L., Simkus, D. N., Elsila, J. E., Glavin, D. P., Parker, E. T., Dworkin, J. P., Hill, D. H., Connolly, H. C., and Lauretta, D. S. 2020. Extraterrestrial Organic Compounds and Cyanide in the CM2 Carbonaceous Chondrites Aguas Zarcas and Murchison. *Meteoritics & Planetary Science* 55: 1509–24.

Basile, B. P., Middleditch, B. S., and Oró, J. 1984. Polycyclic Aromatic Hydrocarbons in the Murchison Meteorite. *Organic Geochemistry* 5: 211–16.

Becker, R. H., and Epstein, S. 1982. Carbon, Hydrogen and Nitrogen Isotopes in Solvent-Extractable Organic-Matter from Carbonaceous Chondrites. *Geochimica et Cosmochimica Acta* 46: 97–103.

Bergameschi, B. A., Tsamakis, E., Keil, R. G., Eglinton, T. I., Montluçon, D. B., and Hedges, J. I. 1996. The Effect of Grain Size and Surface Area on Organic Matter, Lignin and Carbohydrate Concentration, and Molecular Compositions in Peru Margin Sediments. *Geochimica et Cosmochimica Acta* 61: 1247–60.

Budavari, S., Neil, M., Smith, A., Heckelman, P., and Obenchain, J. 1996. *The Merck Index—An Encyclopedia of Chemicals, Drugs, and Biologicals*. Whitehouse Station, NJ: CRC Press.

Cody, G. D., Alexander, C. M. O'D., Foustoukos, D. I., Eckley, S. A., Burton, A. S., Berger, E. L., Neuvo, M., et al. 2023. Testing the Effect of X-Ray Computed Tomography on Chondritic Insoluble Organic Matter and Exploring Parent Body Molecular Evolution. *Meteoritics & Planetary Science*. https://doi.org/10.1111/maps.14096.

Cody, G. D., Alexander, C. M. O'D., and Tera, F. 2002. Solid-State (H-1 and C-13) Nuclear Magnetic Resonance Spectroscopy of Insoluble Organic Residue in the Murchison Meteorite: A Self-Consistent Quantitative Analysis. *Geochimica et Cosmochimica Acta* 66: 1851–65.

Court, R. W., Sephton, M. A., Parnell, J., and Gilmour, I. 2006. The Alteration of Organic Matter in Response to Ionising Irradiation: Chemical Trends and Implications for Extraterrestrial Sample Analysis. *Geochimica et Cosmochimica Acta* 70: 1020–39.

DellaGiustina, D. N., Burke, K. N., Walsh, K. J., Smith, P. H., Golish, D. R., Bierhaus, B., Ballouz, R. L., et al. 2020. Variations in Color and Reflectance on the Surface of Asteroid (101955) Bennu. *Science* 370: eabc3660.

DellaGiustina, D. N., Kaplan, H. H., Simon, A. A., Bottke, W. F., Avdellidou, C., Delbo, M., Ballouz, R. L., et al. 2021. Exogenic Basalt on Asteroid (101955) Bennu. *Nature Astronomy* 5: 31–38.

Ebel, D. S., and Rivers, M. L. 2007. Meteorite 3-D Synchrotron Microtomography: Methods and Applications. *Meteoritics & Planetary Science* 42: 1627–46.

Eckley, S. A., Zeigler, R. A., McCubbin, F. M., Needham, A. W., Fries, M. D., and Gross, J. 2020. Applicability and Utility of the Astromaterials X-Ray Computed Tomography Laboratory at Johnson Space Center. *51st Lunar and Planetary Science Conference*, abstract #2182, JSC-E-DAA-TN77783.

Elsila, J. E., Aponte, J. C., Blackmond, D. G., Burton, A. S., Dworkin, J. P., and Glavin, D. P. 2016. Meteoritic Amino Acids: Diversity in Compositions Reflects Parent Body Histories. *ACS Central Science* 2: 370–79.

Ertem, G., Glavin, D. P., Volpe, R. P., and McKay, C. P. 2021. Evidence for the Protection of N-Heterocycles from Gamma Radiation by Mars Analogue Minerals. *Icarus* 368: 114540.

Friedrich, J. M., Glavin, D. P., Rivers, M. L., and Dworkin, J. P. 2016. Effect of a Synchrotron X-Ray Microtomography Imaging Experiment on the Amino Acid Content of a CM Chondrite. *Meteoritics & Planetary Science* 51: 429–437.

Friedrich, J. M., McLain, H. L., Dworkin, J. P., Glavin, D. P., Towbin, W. H., Hill, M., and Ebel, D. S. 2019. Effect of Polychromatic X-Ray Microtomography Imaging on the Amino Acid Content of the Murchison CM Chondrite. *Meteoritics & Planetary Science* 54: 220–28.

Friedrich, J. M., Ruzicka, A., Rivers, M. L., Ebel, D. S., Thostenson, J. O., and Rudolph, R. A. 2013. Metal Veins in the Kernouve (H6 S1) Chondrite: Evidence for Pre- or Syn-Metamorphic Shear Deformation. *Geochimica et Cosmochimica Acta* 116: 71–83.

Friedrich, J. M., Weisberg, M. K., and Rivers, M. L. 2014. Multiple Impact Events Recorded in the NWA 7298 H Chondrite Breccia and the Dynamical Evolution of an Ordinary Chondrite Asteroid. *Earth & Planetary Science Letters* 394: 13–19.

Furukawa, Y., Chikaraishi, Y., Ohkouchi, N., Ogawa, N. O., Glavin, D. P., Dworkin, J. P., Abe, C., and Nakamura, T. 2019. Extraterrestrial Ribose and Other Sugars in Primitive Meteorites. *Proceedings of the National Academy of Sciences of the United States of America* 116: 24440–45.

Glavin, D. P., Alexander, C. M. O'D., Aponte, J. C., Baczynski, A. A., Berger, E. L., Burton, A. S., Cody, G. D., et al. 2023. Investigating the Impact of X-Ray Computed Tomography Imaging on Organic Matter in the

Murchison Meteorite: Implications for Bennu Sample Analyses (abstract #1030). *54th Lunar and Planetary Science Conference*, The Woodlands, Texas. CD-ROM.

Glavin, D. P., Alexander, C. M. O'D., Aponte, J. C., Dworkin, J. P., Elsila, J. E., and Yabuta, H. 2018. The Origin and Evolution of Organic Matter in Carbonaceous Chondrites and Links to their Parent Bodies. In *Primitive Meteorites and Asteroids*, edited by N. Abreu, 205–271. Amsterdan, The Netherlands: Elsevier.

Glavin, D. P., Burton, A. S., Elsila, J. E., Aponte, J. C., and Dworkin, J. P. 2020. The Search for Chiral Asymmetry as a Potential Biosignature in our Solar System. *Chemical Reviews* 120: 4660–89.

Glavin, D. P., Callahan, M. P., Dworkin, J. P., and Elsila, J. E. 2011. The Effects of Parent Body Processes on Amino Acids in Carbonaceous Chondrites. *Meteoritics & Planetary Science* 46: 1–25.

Glavin, D. P., Elsila, J. E., McLain, H. L., Aponte, J. C., Parker, E. T., Dworkin, J. P., Hill, D. H., Connolly, H. C., and Lauretta, D. S. 2021. Extraterrestrial Amino Acids and L-Enantiomeric Excesses in the CM2 Carbonaceous Chondrites Aguas Zarcas and Murchison. *Meteoritics & Planetary Science* 56: 148–173.

Graham, H. V., Elsila, J. E., Dworkin, J. P., Sandford, S. A., and Aponte, J. C. 2022. Deuterium Isotope Fractionation of Polycyclic Aromatic Hydrocarbons in Meteorites as an Indicator of Interstellar/Protosolar Processing History. *Life-Basel* 12: 1368.

Hamilton, V. E., Simon, A. A., Christensen, P. R., Reuter, D. C., Clark, B. E., Barucci, M. A., Bowles, N. E., et al. 2019. Evidence for Widespread Hydrated Minerals on Asteroid (101955) Bennu. *Nature Astronomy* 3: 332–340.

Hammer, P. G., Yi, R. Q., Yoda, I., Cleaves, H. J., and Callahan, M. P. 2019. Radiolysis of Solid-State Nitrogen Heterocycles Provides Clues to their Abundance in the Early Solar System. *International Journal of Astrobiology* 18: 289–295.

Hertkorn, N., Harir, M., and Schmitt-Kopplin, P. 2015. Nontarget Analysis of Murchison Soluble Organic Matter by High-Field NMR Spectroscopy and FTICR Mass Spectrometry. *Magnetic Resonance in Chemistry* 53: 754–768.

Hertzog, J., Naraoka, H., and Schmitt-Kopplin, P. 2019. Profiling Murchison Soluble Organic Matter for New Organic Compounds with APPI- and ESI-FT-ICR MS. *Life-Basel* 9: 48.

Huang, Y., Aponte, J. C., Tarozo, R., and Hallmann, C. 2015. Hydrogen and Carbon Isotopic Ratios of Polycyclic Aromatic Compounds in Two CM2 Carbonaceous Chondrites and Implications for Prebiotic Organic Synthesis. *Earth and Planetary Science Letters* 426: 101–8.

Jungclaus, G. A., Yuen, G. U., Moore, C. B., and Lawless, J. G. 1976. Evidence for the Presence of Low Molecular Weight Alcohols and Carbonyl Compounds in the Murchison Meteorite. *Meteoritics* 11: 231–37.

Kaplan, H. H., Lauretta, D. S., Simon, A. A., Hamilton, V. E., DellaGiustina, D. N., Golish, D. R., Reuter, D. C., et al. 2020. Bright Carbonate Veins on Asteroid (101955) Bennu: Implications for Aqueous Alteration History. *Science* 370: eabc3557.

Kato, K., Nakayoshi, T., Kurimoto, E., and Oda, A. 2020. Mechanisms of Deamidation of Asparagine Residues and Effects of Main-Chain Conformation on Activation Energy. *International Journal of Molecular Sciences* 21: 7035.

Kminek, G., and Bada, J. L. 2006. The Effect of Ionizing Radiation on the Preservation of Amino Acids on Mars. *Earth & Planetary Science Letters* 245: 1–5.

Kminek, G., Conley, C. A., Allen, C. C., Bartlett, D. H., Beaty, D. W., Benning, L. G., Bhartia, R., et al. 2014. Report of the Workshop for Life Detection in Samples from Mars. *Life Sciences in Space Research* 2: 1–5.

Kvenvolden, K., Lawless, J., Pering, K., Peterson, E., Flores, J., Ponnamperuma, C., Kaplan, I. R., and Moore, C. 1970. Evidence for Extraterrestrial Amino-Acids and Hydrocarbons in the Murchison Meteorite. *Nature* 228: 923–26.

Lauretta, D. S., Adam, C. D., Allen, A. J., Ballouz, R. L., Barnouin, O. S., Becker, K. J., Becker, T., et al. 2022. Spacecraft Sample Collection and Subsurface Excavation of Asteroid (101955) Bennu. *Science* 377: 285–291.

Lauretta, D. S., DellaGiustina, D. N., Bennett, C. A., Golish, D. R., Becker, K. J., Balram-Knutson, S. S., Barnouin, O. S., et al. 2019. The Unexpected Surface of Asteroid (101955) Bennu. *Nature* 568: 55–60.

Le Guillou, C., and Brearley, A. 2014. Relationships between Organics, Water and Early Stages of Aqueous Alteration in the Pristine CR3.0 Chondrite MET 00426. *Geochimica et Cosmochimica Acta* 131: 344–367.

Oba, Y., Takano, Y., Furukawa, Y., Koga, T., Glavin, D. P., Dworkin, J. P., and Naraoka, H. 2022. Identifying the Wide Diversity of Extraterrestrial Purine and Pyrimidine Nucleobases in Carbonaceous Meteorites. *Nature Communications* 13: 2008.

Oba, Y., Takano, Y., Naraoka, H., Watanabe, N., and Kouchi, A. 2019. Nucleobase Synthesis in Interstellar Ices. *Nature Communications* 10: 4413.

Pace, A. L., Wong, R. L., Zhang, Y. T., Kao, Y. H., and Wang, Y. J. 2013. Asparagine Deamidation Dependence on Buffer Type, pH, and Temperature. *Journal of Pharmaceutical Sciences* 102: 1712–23.

Pavlov, A. A., McLain, H. L., Glavin, D. P., Roussel, A., Dworkin, J. P., Elsila, J. E., and Yocum, K. M. 2022. Rapid Radiolytic Degradation of Amino Acids in the Martian Shallow Subsurface: Implications for the Search for Extinct Life. *Astrobiology* 22: 1099–1115.

Pering, K. L., and Ponnamperuma, C. 1971. Aromatic Hydrocarbons in the Murchison Meteorite. *Science* 173: 237–39.

Pizzarello, S., Wang, Y., and Chaban, G. M. 2010. A Comparative Study of the Hydroxy Acids from the Murchison, GRA 95229 and LAP 02342 Meteorites. *Geochimica et Cosmochimica Acta* 74: 6206–17.

Poludniowski, G., Landry, G., DeBlois, F., Evans, P. M., and Verhaegen, F. 2009. SpekCalc: A Program to Calculate Photon Spectra from Tungsten Anode x-Ray Tubes. *Physics in Medicine & Biology* 54: N433–N438.

Rozitis, B., Ryan, A. J., Emery, J. P., Christensen, P. R., Hamilton, V. E., Simon, A. A., Reuter, D. C., et al. 2020. Asteroid (101955) Bennu's Weak Boulders and Thermally Anomalous Equator. *Science Advances* 6: eabc3699.

Schafer, T., Michel, R., Claret, F., Beetz, T., Wirick, S., and Jacobsen, C. 2009. Radiation Sensitivity of Natural Organic Matter: Clay Mineral Association Effects in the Callovo-Oxfordian Argillite. *Journal of Electron Spectroscopy and Related Phenomena* 170: 49–56.

Schmitt-Kopplin, P., Gabelica, Z., Gougeon, R. D., Fekete, A., Kanawati, B., Harir, M., Gebefuegi, I., Eckel, G., and

Hertkorn, N. 2010. High Molecular Diversity of Extraterrestrial Organic Matter in Murchison Meteorite Revealed 40 Years after its Fall. *Proceedings of the National Academy of Sciences of the United States of America* 107: 2763–68.
Schweizer, A. E., Fowlkes, R. L., McMakin, J. H., and White, T. E. J. 1978. Lower Aliphatic Amines. In *Kirk-Othmer Encyclopedia of Chemical Technology*, edited by M. Grayson, 272–283. New York: Wiley-Interscience.
Sears, D. W. G., Sears, H., Ebel, D. S., Wallace, S., and Friedrich, J. M. 2016. X-Ray Computed Tomography Imaging: A Not-So-Nondestructive Technique. *Meteoritics & Planetary Science* 51: 833–38.
Sears, D. W. G., Sehlke, A., Friedrich, J. M., Rivers, M. L., and Ebel, D. S. 2018. X-Ray Computed Tomography of Extraterrestrial Rocks Eradicates their Natural Radiation Record and the Information it Contains. *Meteoritics & Planetary Science* 53: 2624–31.
Simkus, D. N., Aponte, J. C., Elsila, J. E., Parker, E. T., Glavin, D. P., and Dworkin, J. P. 2019. Methodologies for Analyzing Soluble Organic Compounds in Extraterrestrial Samples: Amino Acids, Amines, Monocarboxylic Acids, Aldehydes, and Ketones. *Life-Basel* 9: 47.
Simkus, D. N., Aponte, J. C., Hilts, R. W., Elsila, J. E., and Herd, C. D. K. 2019. Compound-Specific Carbon Isotope Compositions of Aldehydes and Ketones in the Murchison Meteorite. *Meteoritics & Planetary Science* 54: 142–156.
Simon, A. A., Kaplan, H. H., Hamilton, V. E., Lauretta, D. S., Campins, H., Emery, J. P., Barucci, M. A., et al. 2020. Widespread Carbon-Bearing Materials on Near-Earth Asteroid (101955) Bennu. *Science* 370: abc3522.
Takano, Y., Kashiyama, Y., Ogawa, N. O., Chikaraishi, Y., and Ohkouchi, N. 2010. Isolation and Desalting with Cation-Exchange Chromatography for Compound-Specific Nitrogen Isotope Analysis of Amino Acids: Application to Biogeochemical Samples. *Rapid Communications in Mass Spectrometry* 24: 2317–23.
Wilbur, Z. E., Barnes, J. J., Eckley, S. A., Ong, I. J., Brounce, M., Crow, C. A., Erickson, T., et al. 2023. Volatiles, Vesicles, and Vugs: Unraveling the Magmatic and Eruptive Histories of Steno Crater Basalts. *Meteoritics & Planetary Science* 58: 1600–1628.

SUPPORTING INFORMATION

Additional supporting information may be found in the online version of this article.

Figure S1. Video (.mp4 file entitled "MurchisonB_XCT_TIFF_Stack_Video") generated from the continuous series of reconstructed 2D CT slices for the Murchison B sample. The white scale bar shown at the bottom right is 2 mm.

Figure S2. 3D volume rendering video (.mp4 file entitled "MurchisonB_3D_XCT_video") generated from the Murchison B sample reconstructed CT slices using Dragonfly™ volume rendering software. The black scale bar shown at the bottom right is 5 mm.

Figure S3. The 20 to 45 min region of the LC-FD chromatograms (no protein amino acid peaks were observed outside of this retention time range). AccQ·Tag derivatization (10 min) of amino acids in the standard and of the room temperature water extracts after sonication for 1 h of the Murchison A and B samples and the procedural blank. Peaks were identified in the samples by comparison of the UV fluorescence retention time and multiple reaction monitoring (MRM) mass transitions as shown in Table S2 to those in the standards analyzed on the same day and are designated by peak number as follows: (1) histidine; (2) asparagine; (3) glutamine; (4) serine; (5) arginine; (6) glycine; (7) aspartic acid; (8) glutamic acid; (9) threonine; (10) alanine; (11) proline; (12) cysteine; (13) tyrosine; (14) lysine; (15) methionine; (16) valine; (17) leucine; (18) isoleucine; (19) phenylalanine; and (20) tryptophan. All derivatized amino acids were observed in the fluorescence trace except for tyrosine and tryptophan (indicated by asterisks) which were only identified in the standard by mass. Peaks in the chromatograms that are not numbered in the standard are non-protein amino acids which were not quantified as part of this study.

Figure S4. The 1.5 to 9.0 min region of the LC-FD chromatograms (no significant peaks were observed outside of this retention time range). AccQ·Tag derivatization (10 min) of amines in the standard and of the room temperature water extracts after sonication for 1 h of the Murchison A and B samples and the procedural blank. Peaks were identified in the samples by comparison of the UV fluorescence retention time and multiple reaction monitoring mass (MRM) transitions as shown in Table S3 to those in the standard analyzed on the same day and are designated by peak numbers as follows: (1) methylamine; (2) ethylamine; (3) isopropylamine; (4) propylamine; (5) *sec*-butylamine; (6) isobutylamine; (7) *n*-butylamine; (8) *tert*-butylamine; (9) 3-aminopentane; (10) 2-amino-3-methylbutane; (11) *sec*-pentylamine; (12) 2-methylbutylamine; (13) *tert*-pentylamine; (14) isopentylamine; (15) pentylamine; and (16) hexylamine.

Figure S5. Positive electron-impact GC-QqQ-MS chromatograms of the 5.6 to 16.0 min. regions (m/z = 70 ± 0.5) of derivatized carboxylic acids from the hot water extracts of Murchison A and B and the procedural blank, and commercially available standards. Peaks were identified by comparison to the retention times and mass spectra in the samples to the standards analyzed on the same day and are designated by peak number as follows: (1) formic acid; (2) acetic acid; (3) propanoic acid; (4) isobutyric acid; (5) 2,2-dimethylpropanoic acid; (6) butyric acid; (7) 2-methylbutyric acid; (8) isopentanoic acid; (9) 2,2-dimethylbutyric acid; (10) 3,3-dimethylbutyric acid; (11) pentanoic acid; (12) 2-ethylbutyric acid and 2-

methylpentanoic acid; (13) 3-methylpentanoic; (14) 4-methylpentanoic acid; (15) hexanoic acid; (16) benzoic acid; (17) malonic acid; (18) succinic acid; (19) fumaric acid; (20) glutaric acid; (B) derivatization reaction byproduct; and (U) unidentified derivative.

Figure S6. Positive electron-impact GC-QqQ-MS chromatograms of the 17 to 23 min regions (m/z = 101 + 115) of derivatized hydroxy acids from hot water extracts of Murchison A and B and the procedural blank, and commercially available standards. Peaks were identified by comparison to the retention times and mass spectra in the samples to those in the standards analyzed on the same day and are designated by peak number as follows: (1) 2-hydroxyisobutyric acid; (2) (*S*)-lactic acid; (3) (*R*)-2-lactic acid; (4) glycolic acid; (5) (*S*,*R*)-2-hydroxybutyric acid; (6) (*S*)-2-hydroxy-2-methylbutyric acid; (7) (*R*)-2-hydroxy-2-methylbutyric acid; (B) derivatization reaction byproduct; and (U) unidentified derivative.

Figure S7. Single-ion GC-MS chromatograms of the 9 to 19 min regions (m/z = 181.0 ± 0.5) of derivatized carbonyl compounds from hot water extracts of Murchison A and B and the procedural blank, and commercially available aldehyde and ketone standards. For the aldehydes and ketones that have asymmetrical chemical structures, the derivatization reaction yields two chromatographic peaks ((*E*)- and (*Z*)-isomers). The two Murchison chromatograms and the procedural blank chromatogram are on the same intensity scale. Peaks were identified by comparison to the retention times and mass spectra in the samples to those in the standards analyzed on the same day and are designated by peak number as follows: (1) formaldehyde; (2) (*E*)-acetaldehyde; (3) (*Z*)-acetaldehyde; (4) acetone; (5) (*E*)-propionaldehyde; (6) (*Z*)-propionaldehyde; (7) (*E*)-2-butanone; (8) (*Z*)-2-butanone; (9) (*E*)-butyraldehyde; (10) (*Z*)-butyraldehyde; (11) (*E*)-2-pentanone; (12) (*Z*)-2-petanone; (13) (*E*)-2-hexanone; (14) (*Z*)-2-hexanone; (15) (*E*)-benzaldehyde; and (16) (*Z*)-benzaldehyde. The upper end of Peak *R*, which represents unreacted PFBHA derivatization reagent, was not included in the figure to focus on the smaller peaks corresponding to derivatized aldehydes and ketones.

Figure S8. Positive electron-impact total ion current GC-QqQ-MS chromatograms of the 20 to 30 min regions of PAHs from 9:1 DCM:MeOH extracts of Murchison A and B and the procedural blank, and commercially available standards. Peaks were identified in the samples by comparison to the retention times and mass spectra to those in the standard analyzed on the same day and are designated by peak number as follows: (1) acenaphthene; (2) phenanthrene; (3) fluoranthene; and (4) pyrene.

Figure S9. Single-ion GC-QqQ-MS chromatograms of the 11 to 18 min regions (m/z = 166.0 ± 0.5) of *S*-TPC derivatized alcohols in the DCM extracts of Murchison A and B and the procedural blank, and commercially available standards. The two Murchison chromatograms and the procedural blank chromatogram are on the same intensity scale. The intensity of the trace for compounds eluting after 14.5 min in the Murchison samples and procedural blank was magnified by a factor of 20 to improve the clarity of the smaller peaks. Peaks were identified in the samples by comparison to the retention times and mass spectra to those in the standards analyzed on the same day and are designated by peak number as follows: (1) methanol; (2) ethanol; (3) isopropanol; (4) *tert*-butanol; (5) *n*-propanol; (6) (*R*)-(-)-2-butanol; (7) (*S*)-(+)-2-butanol; (8) *n*-butanol; (9) (*R*)-(-)-3-methyl-2-butanol; (10) (*S*)-(+)-3-methyl-2-butanol; (11) (*R*)-(-)-2-pentanol; (12) (*S*)-(+)-2-pentanol; (13) 3-pentanol; (14) 3-methyl-1-butanol; (15) *n*-pentanol; (16) 4-methyl-1-pentanol; (17) 3-methyl-1-pentanol; and (18) *n*-hexanol. The peaks labeled *R* represent unreacted *S*-TPC derivatization reagent.

Figure S10. The 35 to 43 min region of the single ion (m/z = 115) chromatograms from the GC-MS analyses of pentose derivatives in the water and 2% HCl extracts of Murchison A and B samples and serpentine blanks, and a standard. Peaks in the samples were identified by comparison of the retention times and mass spectra to those in the standard analyzed on the same day and are designated by peak number as follows: (1) ribose; (2) lyxose; (3) arabinose; and (4) xylose.

Figure S11. High resolution mass chromatograms of nitrogen heterocycles in the Murchison A and B and serpentine blank extracts, as well as standards at the mass to charge (m/z) ratios corresponding to: (a) uracil; (b) thymine; (c) monoamino-monohydroxypyrimidine; (d) ethyluracil; (e) adenine; (f) hypoxanthine; and (g) guanine; and (h) xanthine. Peaks were identified in the samples by comparison of the retention time and molecular mass to those in standards analyzed on the same day and are designated by peak number as follows: (1) uracil; (2) 1-methyluracil; (3) thymine; (4) 4-amino-5-hydroxypyrimidine; (5) 4-amino-6-hydroxypyrimidine; (6) 5,6-dimethyluracil; (7) 5-ethyluracil;(8) adenine; (9) hypoxanthine; (10) guanine; (11) isoguanine; and (12) xanthine.

Figure S12. High resolution mass chromatograms of nitrogen heterocycles in the Murchison A and B and serpentine blank extracts, as well as standards at the mass to charge (m/z) ratios corresponding to: (i) purine; (j) diaminopurine; (k) imidazolecarboxylic acid; (l) nicotinamide; (m) nicotinic acid; (n) monomethyl-imidazole carboxylic acid; (o) methylnicotinamide; and (p) methylnicotinic acid. Peaks were identified in the samples by comparison of the retention time and molecular mass to those in standards analyzed on the same day and are

designated by peak number as follows: (13) purine; (14) 2,6-diaminopurine; (15) 4-imidazolecarboxylic acid; (16) 2-imidazolecarboxylic acid; (17) nicotinamide; (18) picolinamide; (19) isonicotinic acid; (20) nicotinic acid; (21) 1-methyl-1H-imidazole-5-carboxylic acid; (22) 1-methyl-1H-imidazole-2-carboxylic acid; (23) 4-methyl-1H-imidazole-5-carboxylic acid; (24) 5-methylnicotinamide; (25) 2-methylnicotninic acid; (26) 4-methylnicotinic acid; (27) 6-methylnicotinic acid; and (28) 5-methylnicotinic ac id.

Figure S13. Nontargeted screenings of Murchison A and B MeOH extracts analyzed with ESI(+)-FTICR-MS. (a) Van Krevelen diagrams of annotated molecular formulae classified as CH, CHN, CHS, CHO, CHNO, CHOS, or CHNOS. Neutral molecular formulae are plotted. The bubble size indicates the mean relative intensities of corresponding peaks in the spectra. The donut plot shows the distribution of all chemical spaces and total annotated molecular formulae. (b) Oxygen frequency in CHO, CHOS and CHNO. (c) Sulfur and nitrogen frequency in CHOS and CHNO, respectively.

Figure S14. Nontargeted screenings of Murchison A and B MeOH extracts analyzed with APPI(+)-FTICR-MS. (a) Van Krevelen diagrams of annotated molecular formulae classified as CH, CHN, CHS, CHO, CHNO, CHOS, or CHNOS. Neutral molecular formulae are plotted. The bubble size indicates the mean relative intensities of corresponding peaks in the spectra. The donut plot shows the distribution over all chemical spaces and total annotated molecular formulae. (b) Oxygen frequency in CHO, CHOS and CHNO. (c) Sulfur and nitrogen frequency in CHOS and CHNO, respectively.

Figure S15. Comparison of the chemical spaces in the hexane, DCM, MeOH and water extracts of Murchison A and B analyzed with ESI(−)-FTICR-MS. Van Krevelen diagrams of annotated molecular formulae classified as CHO, CHNO, CHOS, or CHNOS. Neutral molecular formulae are also plotted. The bubble size indicates the mean relative intensities of corresponding peaks in the spectra. The donut plot shows the distribution over all chemical spaces and total annotated molecular formulae.

Table S1. Summary of the results from the specific surface area ($m^2\ g^{-1}$) measurements of the Murchison A and B residue pairs calculated from the slopes of the linear fits of the 5 pt. BET isotherms and sample masses after solvent extraction of the protein amino acids and amines, PAHs, and alcohols.

Table S2. Multiple reaction monitoring (MRM) parameters used for the LC-QqQ-MS peak quantifications of the AccQ·Tag derivatives of the 20 standard protein amino acids.

Table S3. Multiple reaction monitoring (MRM) parameters used for the LC-QqQ-MS peak quantifications of the AccQ·Tag derivatives of the amines.

Data S1. Excel file containing all data points used to generate the plots shown in Figure 13 and Figures S3–S15.